



ELSEVIER

Contents lists available at ScienceDirect

Quaternary Science Reviews

journal homepage: www.elsevier.com/locate/quascirev

Palaeoenvironmental implications from Lower Volga loess - Joint magnetic fabric and multi-proxy analyses

Chiara Költringer^{a, *}, Balázs Bradák^b, Thomas Stevens^a, Bjarne Almqvist^a, Adriano Banak^c, Martin Lindner^d, Redzhep Kurbanov^{e, f}, Ian Snowball^a

^a Uppsala University, Department of Earth Sciences, 75236, Villavägen 16, Sweden

^b Graduate School of Maritime Sciences, Kobe University, 5-1-1 Fukaeminami-machi, Higashinada-ku, Kobe 658-0022, Japan

^c Croatian Geological Survey, Department for Geology, Sachsova 2, Zagreb, Croatia

^d University of Salzburg, Department of Chemistry and Physics of Materials, Jakob-Haringer-Straße 2a, 5020, Salzburg, Austria

^e MSU, Lomonosov Moscow State University, Faculty of Geography, M.V., Leninskie Gori, 1, Moscow, 119992, Russia

^f RAS, Laboratory of Evolutionary Geography, Institute of Geography, Staromonetny, 29, Moscow, 119017, Russia

ARTICLE INFO

Article history:

Received 16 November 2020

Received in revised form

17 June 2021

Accepted 22 June 2021

Available online 30 July 2021

Handling Editor: Xiaoping Yang

Keywords:

Anisotropy of magnetic susceptibility

Scanning electron microscopy

Loess

Northern Caspian Sea region

Palaeowinds

Post-depositional reworking

Chemical alteration

Palaeoclimate reconstruction

ABSTRACT

Magnetic fabric (MF) investigations complemented by geochemical and grain surface analyses of the understudied and controversial marine isotope stage (MIS) 5 b, 4 and 3 loess deposits in the Lower Volga region, Russia show that the material has been transported and deposited by wind and to a large extent experienced post-depositional reworking. Grain surface features suggest that the material was glacially ground and fluvially transported prior to final aeolian deposition as loess. Secondary magnetic fabrics in the loess reveal pedogenic and cryogenic processes and a generally cold environment with brief shifts to warmer climate during late MIS 5 and MIS 3. Palaeowind reconstructions derived from preserved primary aeolian MF, indicate locally influenced westerly and north-westerly flow as part of a wider scale westerly wind pattern, similar to modern day winter conditions. We suggest that the climate of the last glacial in the Northern Caspian Lowland was cold and dry, with higher windspeeds and less variability during MIS 4 compared to MIS 3.

© 2021 The Authors. Published by Elsevier Ltd. This is an open access article under the CC BY license (<http://creativecommons.org/licenses/by/4.0/>).

1. Introduction

Loess deposits in the Northern Caspian Sea region play a significant role in understanding continental scale palaeoclimate systems in Eurasia during the Pleistocene. In contrast to the well-studied loess areas of Europe, Central and East Asia, loess in the Northern Caspian lowland has received very little research attention. Despite this lack of attention, its geographical position and the lack of other palaeoenvironmental data from continental deposits in the region (Költringer et al., 2020) make it an important 'missing link' for developing a full understanding of Eurasian palaeoclimate and wind systems. In particular, the deposits in the Lower Volga region (Lower Volga Loess - LVL) that accumulated during marine

isotope stages (MIS) 5, 4 and 3 (Yanina et al., 2017) contain a detailed palaeoclimate archive (Költringer et al., 2020). Reconstruction of prevailing dust transport and wind directions from these deposits would help to unravel the influence of local, regional and hemispheric atmospheric systems on aeolian activity and provide insight into their past variation. However, debate continues about the origin and alteration of LVL, which limits specific past climate parameter reconstruction from the deposits (Költringer et al., 2020). Post-depositional pedogenic and cryogenic processes are suspected to have altered the originally aeolian LVL (Lebedeva et al., 2018; Költringer et al., 2020; Taratunina et al., 2020) or even interfered with its formation (Goretskiy, 1958). Indeed, cryogenic, pedogenic, and slope processes are discussed as alternative formation mechanisms, rather than an aeolian origin (Goretskiy, 1958; Lavrushin et al., 2014) (Supp. Table 1). As a consequence of this debate, the material has seldom been referred to as aeolian loess and has been neglected as a palaeoclimate archive (Költringer

* Corresponding author.

E-mail address: chiara.koltringer@geo.uu.se (C. Költringer).

et al., 2020).

Palaeowind directions and loess forming processes have been identified based on magnetic fabric (MF) analyses in different loess regions (Lagroix and Banerjee, 2002, 2004b; Zhu et al., 2004). MF in loess occurs due to the mechanical ordering of magnetic minerals, where an air current orients grains into shape preferred orientation (SPO) and results in magnetic anisotropy (Tarling and Hrouda, 1993). Following the early studies of anisotropy of low field magnetic susceptibility (AMS) of loess by Liu et al. (1988), Lagroix and Banerjee (2002, 2004b) as well as Zhu et al. (2004) demonstrated the applicability of AMS for poorly consolidated, non-lithified sediments such as loess and highlighted the potential of this method to reveal palaeowind directions and various surface processes (reworking and redeposition), even for samples with low anisotropy. Palaeowind information has been extracted from loess, which is characterized by flow-aligned, primary aeolian MF (e.g., Siberia (Matasova et al., 2001), Alaska (Lagroix and Banerjee, 2002, 2004b), Chinese Loess Plateau (Zhu et al., 2004; Zhang et al., 2010), Poland and Ukraine (Nawrocki et al., 2006), and Hungary (Bradák, 2009)).

AMS measurements can also help to determine secondary processes that alter the primary, aeolian magnetic fabric (e.g., Hus, 2003; Lagroix and Banerjee, 2004a). The characteristics of the secondary fabric (i.e., the reworked and/or redeposited fabric) can indicate certain environmental conditions, such as pedogenesis, waterlogging, and permafrost activity. Reworking results in the alteration of aeolian fabric without significant transportation, and can be caused by biogenic and cryogenic activity for example. Matasova et al. (2001) and Bradák et al. (2011) uncovered a random distribution of magnetic grains for horizons that have previously experienced bioturbation, as evident from field observation. Realignment of the primary fabric following redeposition under flow or mass movement may also cause significant change. Liu et al. (1988) reported water-lain and redeposited loess that showed a greater degree of anisotropy compared to aeolian loess. Redeposition on a slope by colluvial sedimentation or solifluction is also reported to lead to an inclined MF, with its long principal axes deviating from the horizontal (Matasova et al., 2001).

Together with the flow-aligned fabric, "anomalous" MF, such as flow-transverse (or biaxial prolate) and biaxial oblate fabric, can be observed for loess that otherwise does not display signs of pedogenesis. Flow-transverse MF can develop during high energy aeolian or water-lain transport, which causes the grains to roll and orient themselves with the lineation perpendicular to the flow direction (Bradák et al., 2018a, 2019).

Permafrost processes can alter sediment magnetic fabric in various ways. Biaxial prolate magnetic fabric can form by freeze-thawing related shear stresses during permafrost degradation (Alaskan loess; Lagroix and Banerjee, 2004a). In the actual permafrost state, loess behaves as rigid material, causing rotation/faulting, and leading to the formation of biaxial prolate MF (Lagroix and Banerjee, 2004a). Permafrost below the active layer acts as an impermeable boundary to water (Williams and Smith, 1989), so that groundwater flow is channelled within the active layer. Such groundwater flow or freeze-thawing related solifluction can result in a greater degree of anisotropy (Lagroix and Banerjee, 2004a).

Given the large array of potential processes and fabrics that can be found in loess, magnetic measurements should be combined with other analytical methods in order to help characterize the environment that prevailed during loess formation. X-ray fluorescence (XRF) analysis is a reliable tool to determine chemical composition and test for soil formation or other post depositional chemical alteration (e.g. Buggle et al., 2011). The elemental composition of loess changes with weathering, depleting soluble and mobile elements and, therefore, enriching immobile ones

(Buggle et al., 2008 and the references therein). Additionally, grain shape, surface morphology, and microtexture (micron-sized features in the surface of the grains) of quartz can be used as "fingerprints" for different types of transport (Vos et al., 2014 and the references therein). Here we present results from AMS derived magnetic fabric analyses of LVL, complemented by XRF and scanning electron microscope (SEM) analyses to constrain the environmental conditions and processes operating during loess formation in the LVL. Specifically, we determine the origin and degree/type of reworking of LVL deposits, reconstruct palaeowind directions, and use this information to constrain local versus large-scale synoptic wind patterns in the Northern Caspian lowland.

2. Site and sampling

The Lower Volga region is located within the large plain of the Northern Caspian lowland in the south of Russia (Fig. 1). Loess deposits crop out in sections along incised gullies, river and stream channels in this area, typically representing the classic regional stratigraphy, including marine deposits from two Caspian Sea transgressions (Khazarian and Kvalynian) and continental ones from the intervening regression phase (Atelian) (e.g. Yanina, 2014; Tudryn et al., 2013). The loess itself deposited during the Atelian stage of Caspian Sea sea-level lowstand, which has been dated to ~25–85 ka, corresponding MIS 5b–3 (Yanina et al., 2017), and is confined by the transgressive marine sediments at the bottom and the top (Yanina, 2014; Lebedeva et al., 2018; Költringer et al., 2020). The Atelian represents a time period of cold and dry climate in the Northern Caspian lowland, dominated by grass steppe vegetation. Estimated palaeoprecipitation is 300–400 mm/a, indicating a semi-arid environment (Költringer et al., 2020). Signs of cryogenic processes and pedogenesis are reported for the Atelian deposits (Goretskiy, 1958; Yanina, 2014; Lebedeva et al., 2018; Költringer et al., 2020; Taratunina et al., 2020). The studied section at Leninsk (LN) is located about 60 km east of the city of Volgograd (48.7213 N, 45.1592 E, WGS 48) and comprises of two natural outcrops: the 14 m thick LN1 and the underlying 3 m thick LN2, which stratigraphically follows below the deeper part of LN1, 350 m further south in a dry gully. The Leninsk stratigraphy comprises fluvial deposits at its base, followed by the loess sequence, which is unconformably separated from overlying marine deposits (Fig. 1), in line with the regional stratigraphic model. A stratigraphic description of Leninsk and the detailed rock magnetic analysis of the sequence can be found in Költringer et al. (2020), who reinforce that the loess at Leninsk represents an aeolian accumulation of fine-grained material based on its sedimentological and magnetic properties. Their initial grain size data and assignment of the Atelian sediment as loess is reinforced by Lebedeva et al. (2018) and Taratunina et al. (2020), who report clear loess characteristics based on detailed soil and cryo-feature analyses, including particle size analysis.

Oriented samples were planned to be taken at stratigraphic intervals of ca. 10 cm from the cleaned loess section (LN1: 7–14 m; LN2: 0–3 m) (Fig. 3). Where the nature of the loess and the accessibility of the section did not allow the sampling of undisturbed oriented samples, the interval had to be increased. The actual spacing between each oriented sample is shown in Fig. 3 and Supp. Table 3. The sampling was undertaken by manually carving oriented cubes of 7 cm³ directly into plastic containers without forceful pushing of the sample, to avoid sampling induced deformation, which could potentially lead to a deflection of the magnetic lineation (Jordanova et al., 1996). In total, 107 oriented samples were obtained, including three samples from wedge infill material (Fig. 3). Bulk samples from every ~50 cm were selected for XRF analysis and bulk samples for SEM grain image analyses were taken

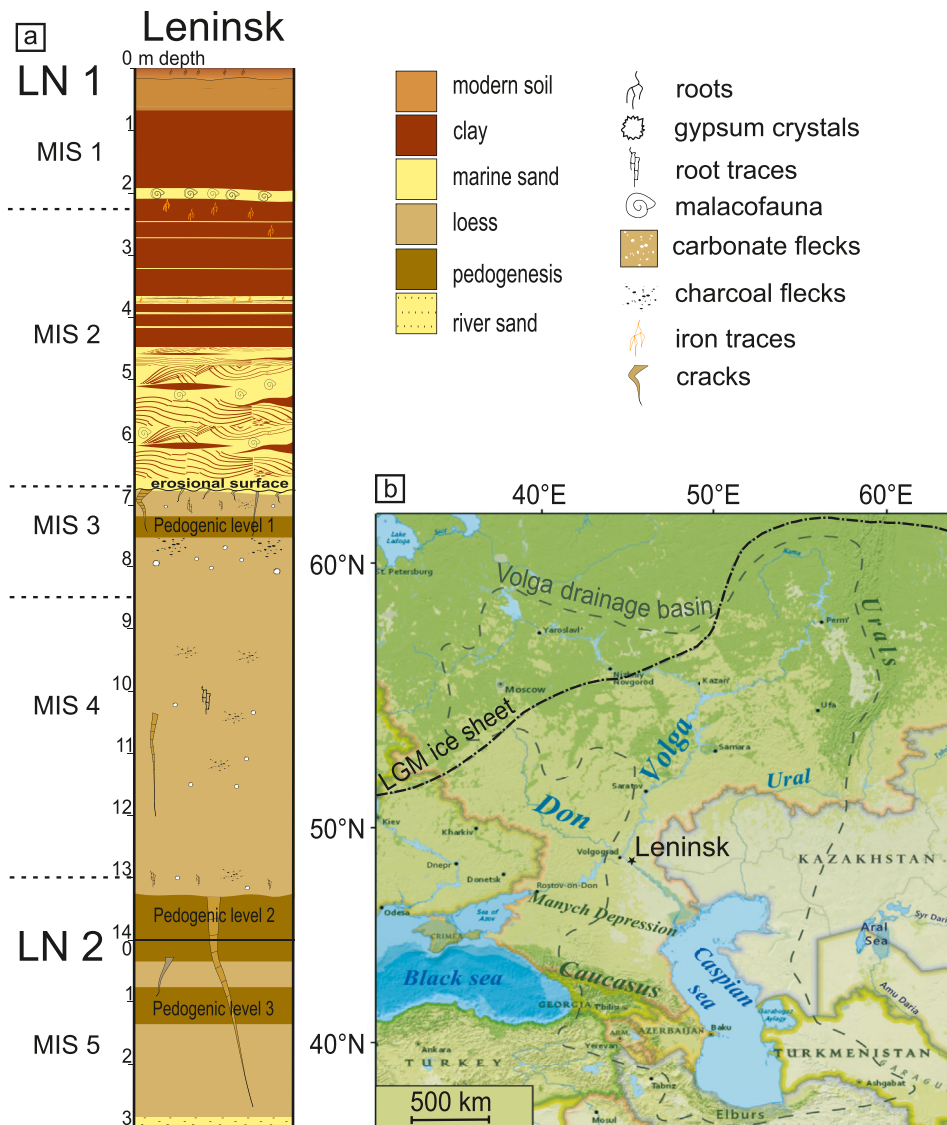


Fig. 1. Stratigraphic chart of Leninsk section (a) and its location in the Russian Northern Caspian lowland (b) (modified after Költringer et al., 2020). The extend of the last glacial maximum ice sheet is shown after Arkhipov et al. (1995).

every metre (Fig. 3), as well as from one Pleistocene Volga sand section around 100 km south of Leninsk (Chorny Yar).

3. Methods

3.1. Magnetic fabric study

The AMS of the oriented samples was measured using an MFK1-FA Kappabridge instrument (AGICO, Czech Republic) equipped with a semi-automated 1-axis sample rotator (Pokorný et al., 2011), using a field of 200 A/m at 976 Hz frequency. The following magnetic anisotropy parameters were calculated using the maximum, intermediate and minimum principal susceptibility axes ($\kappa_{max} \geq \kappa_{int} \geq \kappa_{min}$). A set of magnetic anisotropy parameters (Supplementary Table 3) was calculated with the Anisoft 4.2 software (Chadima and Jelínek, 2008). The mean susceptibility (κ_m) is defined as the arithmetic mean of κ_{max} , κ_{int} and κ_{min} .

Magnetic lineation (L), defined by the alignment of κ_{max} , and

foliation (F) are expressed as (Tarling and Hrouda, 1993):

$$L = \frac{\kappa_{max}}{\kappa_{int}} \quad \text{Eq.1}$$

$$F = \frac{\kappa_{int}}{\kappa_{min}} \quad \text{Eq.2}$$

The corrected degree of anisotropy of magnetic susceptibility (P_j) is defined as follows:

$$P_j = \exp \sqrt{2 \left[(\eta_{max} - \eta_m)^2 + (\eta_{int} - \eta_m)^2 + (\eta_{min} - \eta_m)^2 \right]} \quad \text{Eq.3}$$

where the η parameters are the natural logarithm of principal susceptibility values (i.e., $\eta_{max} = \ln \kappa_{max}$).

The shape parameter T

$$T = \frac{2 * (\eta_{int} - \eta_{max} - \eta_{min})}{(\eta_{max} - \eta_{min})} \quad \text{Eq.4}$$

serves to identify oblate ($1 > T > 0$) or prolate ($-1 < T < 0$) shape of the susceptibility ellipsoid; $T = 0$ signalizes triaxial neutral shape. The relationship between T and P_j is represented in the T versus P_j (Jelínek) diagram.

For the evaluation of the statistical significance of the magnetic parameters of each sample and to check for the presence of significant anisotropy for palaeowind analysis, the parameters F_{12} and F_{23} are considered (Supp. Table 3), following the method suggested by Zhu et al. (2004). F_{12} and F_{23} are based on the F -test for anisotropy (Jelínek, 1977) and allow distinguishing between rotational oblate ($\kappa_{max} = \kappa_{int}$), rotational prolate ($\kappa_{int} = \kappa_{min}$), or triaxial neutral ($\kappa_{max} \neq \kappa_{int} \neq \kappa_{min}$) anisotropy. F_{12} describes the strength of the anisotropy testing in the plane containing the maximum (κ_{max}) and intermediate principal susceptibility (κ_{int}) axes, where instead F_{23} is used in regards to the plane κ_{int} - κ_{min} (Jelínek, 1977). One way of performing the test is by means of confidence angles. E_{12} indicates the variation of κ_{max} in the plane of κ_{max} and κ_{int} and represents the 95% confidence angle for the azimuth of κ_{max} (Zhu et al., 2004; Lagroix and Banerjee, 2004b). Generally, the degree of anisotropy observed in loess is often small and P_j values between 1 and 1.04 are not uncommon (e.g. Bradák et al., 2019). Several studies demonstrated that samples of such values can be considered as significantly anisotropic as long as they pass the statistical evaluation described above (e.g. Zhu et al., 2004; Peng et al., 2015).

3.1.1. Key parameters during the identification of primary aeolian versus secondary magnetic fabric

We adopt criteria to identify primary aeolian MF based on Hus (2003), Lagroix and Banerjee (2004b) and Zhu et al. (2004):

Statistical evaluation. Samples showing significant magnetic foliation ($F_{23} > 10^\circ$) and “classic aeolian characteristics” (sub-horizontal κ_{max} and vertical κ_{min}) for sub-horizontally deposited loess, are identified as showing primary MF, while samples deviating from this, with κ_{min} inclination $< 70^\circ$, are interpreted to show secondary MF (Lagroix and Banerjee, 2004b; Nawrocki et al., 2006). Such identified primary aeolian MF is suitable for palaeowind reconstructions in cases where a significant magnetic lineation is present ($F_{12} > 4^\circ$, $E_{12} < 20^\circ$).

Foliation control. F is clearly higher than L in aeolian MF (Lagroix and Banerjee, 2002). P_j shows a very similar trend to F plotted against depth, indicating the control of F of the shape of the AMS ellipsoid (Zhu et al., 2004).

Stereoplot analysis and the principal susceptibility axes. Aeolian samples show diagnostic MF characteristics, such as orientation of the lineation and the foliation plane (indicated by the principal susceptibility axes), representing gravity controlled and flow-aligned MF (e.g. Bradák et al., 2019). The very gentle dipping of κ_{max} ($< 20^\circ$) as well as the clustering and almost 90° dip of κ_{min} may also reflect an aeolian fabric on a horizontal depositional plain (e.g. Lagroix and Banerjee, 2004b). In addition, secondary sedimentary and subordinately vertically oriented MF may be present and identifiable through the orientation distributions of a representative set of samples in a loess unit. Secondary MF can be subdivided by considering the orientation and association of κ_{max} and κ_{int} . Samples characterized by sub-horizontal κ_{min} and steep dipping κ_{max} show vertically oriented (inverse) MF.

Shape of the susceptibility ellipsoid. Oblate susceptibility ellipsoids, indicated by their positive T , may represent gravitation dominated primary MF (Hus, 2003; Bradák et al., 2011, 2019), potentially affected by depositional or compactional loading (Dubey, 2014; Hus, 2003).

Equal area projection stereoplots in a geographical coordinate system were created using the program Anisoft 4.2 (Chadima and Jelínek, 2008).

3.2. XRF and SEM analyses

The samples were analysed for major and selected trace elements using a Bruker Pioneer S4 crystal spectrometer (Department for Chemistry and Physics of Materials, University of Salzburg), using the procedure of Lindner and Finger (2018). Loss on ignition (LOI) was gravimetrically determined after heating the dried samples to 1100°C for 3 h. The data can be found in Supp. Table 3. To assess the degree of feldspar weathering, the Chemical Index of Alteration is used (CIA; Nesbitt and Young, 1982):

$$CIA = \left(\frac{Al_2O_3}{(Al_2O_3 + CaO + Na_2O + K_2O)} \right) * 100 \quad \text{Eq.6}$$

molar proportions and silicate-only Ca following the assumption of McLennan (1993).

A JEOL, model JSM-35 CF, SEM was used for SEM analysis (13 samples; Croatian Geological Survey, Zagreb). The light mineral fraction was extracted using the Wilfley water table (Pullen et al., 2011). Sample preparation might have an effect on the recovered grain size of the light fraction. For one sample fractions both $>$ and $< 450\ \mu\text{m}$ were separated by dry sieving. More than 700 grains were photographed and complete ones were analysed (magnification range of X20–X1600). Selected grains were mounted onto double-sided adhesives, and then coated with a 15 nm thick gold layer. In this study, the quartz grain surface microtexture classification and terminology used are based on Mahaney (1995, 2002) and Vos et al. (2014).

3.3. Modern wind data analyses

Modelled hourly wind data from 1989 to 2019 were obtained from the reanalysis ERA5 with horizontal resolution of 31 km (Hersbach et al., 2020). Wind speed and wind direction were calculated from the zonal respectively meridional wind speed (u - and v component).

4. Results

4.1. Characterization of the magnetic fabric

Seventy six of the 107 analysed samples show statistically significant magnetic lineation with $F_{12} > 4^\circ$ and $E_{12} < 20^\circ$ (Fig. 2a, Supp. Table 3), despite low values in general (Zhu et al., 2004). As expected, E_{12} shows an inverse relationship to L and independence from P_j and F (Lagroix and Banerjee, 2004b, Fig. 2b–d). No clear correlation between F_{12} and κ_m can be observed (Fig. 2e). A well-resolved magnetic foliation ($F_{23} > 10^\circ$) (Zhu et al., 2004) is seen in the vast majority of samples (Fig. 2f). P_j and κ_m show no clear relationship (Fig. 2g).

4.1.1. The vertical distribution of AMS parameters

Based on the vertical depth variation of the AMS parameters of the 107 samples, three different types of units can be distinguished. The regular unit is described as such due to its uniformity and little signs of post-depositional disturbance. Irregular units in contrast are characterized due to the deviation of their AMS parameters compared to the R unit, as well as their depth variation. Pedogenic units are based on the identification of pedogenic layers in the section. Following this classification, the following units are subdivided (Fig. 3; Supp. Table 2):

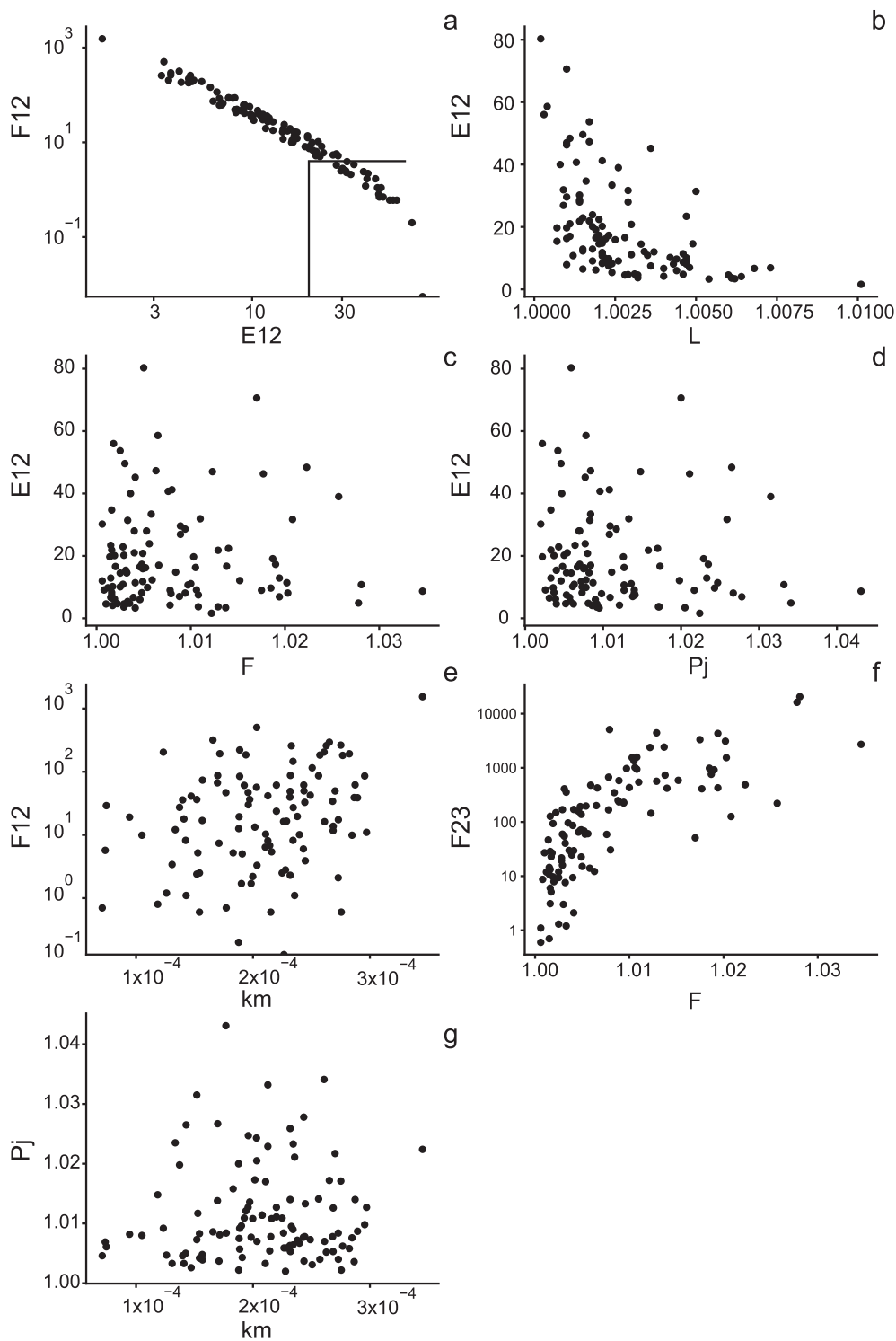


Fig. 2. Statistical evaluation of the AMS data for palaeowind analyses following Lagroix and Banerjee (2004b) and Zhu et al. (2004): (a) identification of statistically significant magnetic lineation ($F_{12} > 4^\circ$ and $E_{12} < 20^\circ$), (b) relationship of E_{12} and L , (c) relationship of E_{12} and F , (d) relationship of E_{12} and P_j , (e) relationship of F_{12} and κ_m , (f) identification of statistically significant magnetic foliation ($F_{23} > 10^\circ$), (g) relationship of P_j and κ_m .

The regular AMS unit (R). The thickest unit is characterized as “regular” (R, 789–1214, 40 samples) by the small vertical variation for most AMS parameters (F , L , P_j) and mostly positive T (Fig. 3). 28 out of 40 samples display oblate T . P_j , F and L are fairly uniform throughout the whole unit and a steep inclination of κ_{\min} (50 – 90°) is seen in 27 samples (Fig. 4, Table 1). The R layer is characterized by

low P_j values, indicating an average anisotropy below 1%, and relatively uniform high κ_m values in contrast to samples from most other layers (Fig. 4, Supp. Table 2).

The palaeosol AMS units (P1–P3). Two of the pedogenic horizons in the profile (described by Költringer et al., 2020) show similar trends for F , P_j , and T , whereas the third palaeosol unit (observed in

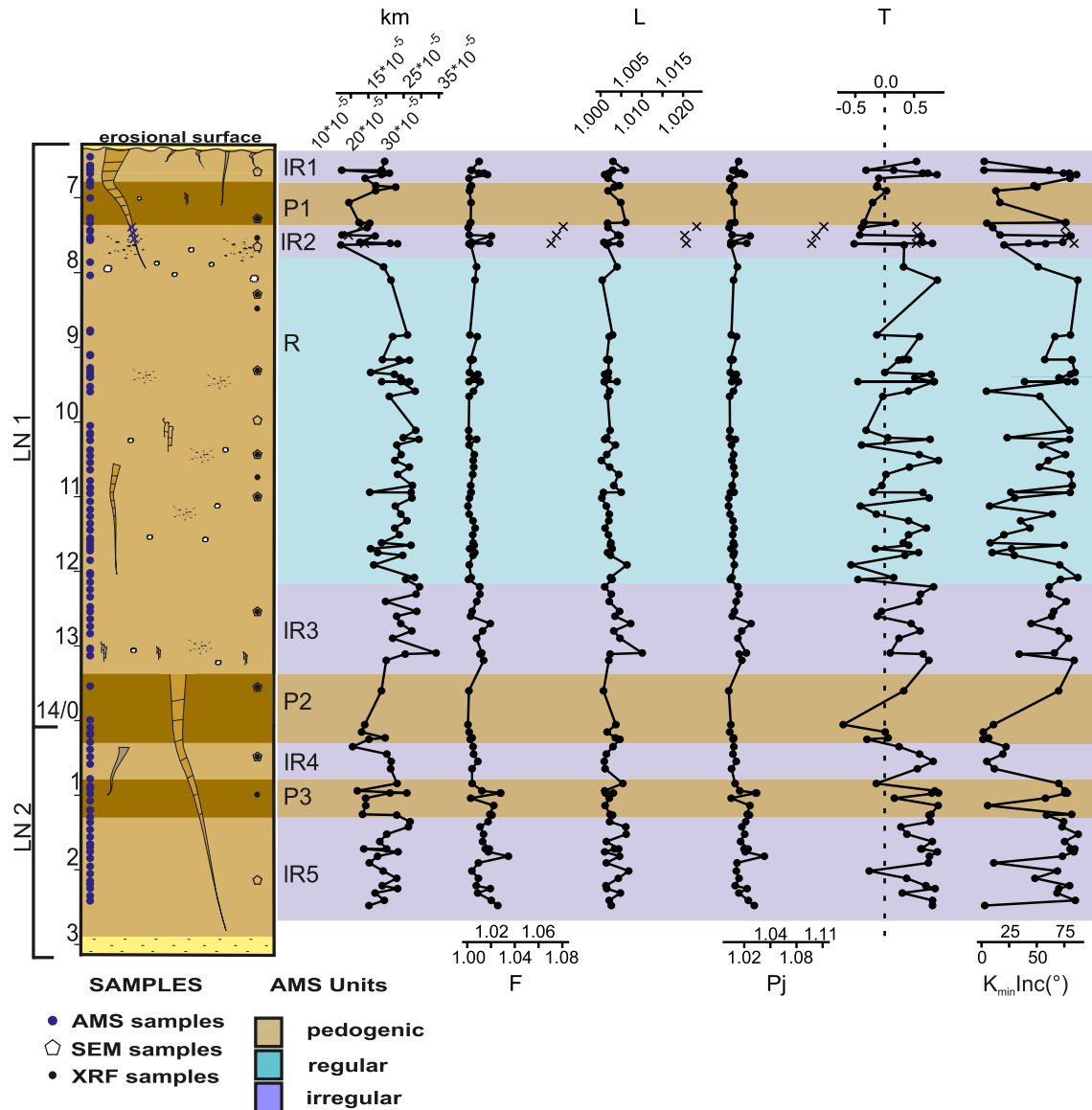


Fig. 3. Sampling points for AMS, SEM and XRF analyses and the vertical variation of magnetic fabric parameters: F, L, Pj, T and κ_{\min} Inclination. The various colors indicate the separated groups of units based on stratigraphy and the behavior of the AMS parameters: "regular" AMS unit (R); pedogenic AMS unit (P1, P2, P3); "irregular" AMS unit (IR1, IR2, IR3, IR4, IR5, for detailed information about the magnetic fabric characteristics of the groups please see Chapter 4.1). The 3 samples from wedge infill material are not included to the curves but displayed as X symbols. For chart legend see Fig. 1. (For interpretation of the references to colour in this figure legend, the reader is referred to the Web version of this article.)

the field) differs in most parameters (Fig. 4). κ_m varies within the pedogenic units but is overall lower than what is measured in most other layers (Figs. 3 and 4, Supp. Table 2).

· Pedogenic unit 1 (P1, 679–730 cm, 6 samples; Fig. 3) features mostly prolate T, where F is generally lower compared to the under- and overlying loess. The overall low but varying Pj reaches max. values of 1.009. L is overall higher than for most other units. The inclination of κ_{\min} varies between 5 and 76° (Figs. 3 and 4; Supp. Table 3). The loess layer directly below P1, representing the parent material of P1 (pm P1), shows lower κ_m , F, L, and Pj than P1. Pm P1 has a prolate character and has shallow inclination of κ_{\min} (Supp. Table 2).

· Pedogenic unit 2 (P2; 1366 cm in LN 1; 0–35 cm in LN 2, 5 samples; Fig. 3) shows partly prolate T. Pj and F are within the range of values observed for unit R. Instead, L shows an average of 1.003, which is relatively high compared to R samples. κ_{\min} inclinations

are preponderantly shallow ($\leq 10^\circ$) with the exception of the only LN1 sample (Fig. 4, Supp. Table 2) and appear to decrease with depth (Fig. 3). The only P2 specimen from LN1 also shows remarkably different behaviour for Pj (1.002) and L (1.0007), which are lower than for the four LN2 samples (Pj: 1.005, 1.003, 1.008, 1.007; L: 1.004, 1.002, 1.005). The parent material in which P2 developed (pm P2) shows higher F and Pj, similar L, lower κ_m , oblate T, and a sub-horizontal κ_{\min} (Supp. Table 2).

· Pedogenic unit 3 (P3; 92–135 cm in LN 2, 8 samples; Fig. 3) exhibits oblate T for 7 samples and higher Pj (max. 1.034) than the other P units. Its κ_m is on average higher but overall comparable to P1 and P2, and lower than for R. L values are higher than in unit R but similar to those from most other units. By contrast, F shows comparably higher values. The κ_{\min} inclination is steep (58–82°) (Fig. 4, Supp. Table 3). The parent material Pm P3 appears different to P3 by exhibiting sub-horizontal κ_{\min} inclination while other

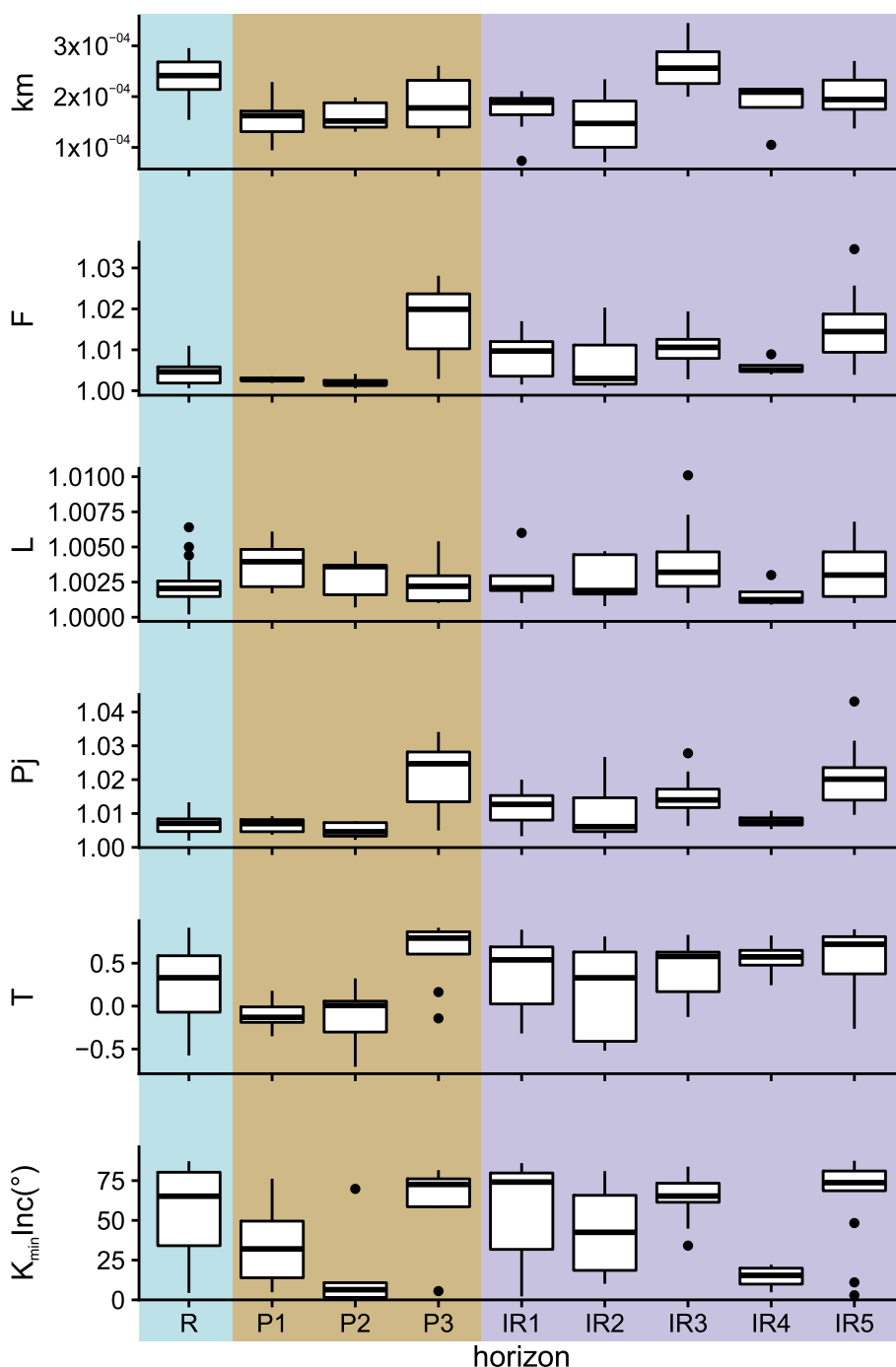


Fig. 4. Box-and-whisker plots of the AMS units for the AMS parameters κ_m , F, L, P_j, T, and κ_{\min} Inclination. The median shows the interquartile range, whiskers indicate maximum and minimum values, outliers are displayed as black points. For colour classification see Fig. 3. (For interpretation of the references to colour in this figure legend, the reader is referred to the Web version of this article.)

parameters are rather similar (Supp. Table 2).

The irregular AMS units (IR1–IR5). In addition to R and the pedogenic units (P1, P2 and P3), five layers are characterized as “irregular” (Figs. 3 and 4, Supp. Table 2):

- Irregular unit 1 (IR1, 642–669 cm, 7 samples; Fig. 3) shows greater variation but overall higher F, L, and P_j than the R group. κ_m by contrast gives lower values. The average anisotropy in IR1 is >1% (Fig. 4, Supp. Table 2). Two samples of IR1 are prolate. The inclination of κ_{\min} shows large variation (min. 2°, max. 80°).

- Irregular unit 2 (IR2, 736–759 cm, 7 samples; Fig. 3) stands out

due to the large variation of most AMS parameters. The average values of F and P_j are higher than those of unit R. The anisotropy of IR1 samples fluctuates between 0.5 and 2% (Fig. 4, Supp. Table 3). κ_m is among the lowest measured in the whole section. Several samples display prolate T. Similarly to IR1, the inclination of κ_{\min} varies considerably (10–81°) (Fig. 4).

- Irregular unit 3 (IR3, 1224–1324 cm, 11 samples; Fig. 3) was defined as irregular due to its high L, F, and P_j compared to unit R. Its κ_m is the highest of all units. The anisotropy in IR3 ranges between 1 and 3%. T is oblate for 9 samples (Figs. 3 and 4; Supp.

Table 1
SEM results and their interpretation.

Section	Sample ID	Group	Depth (cm)	SEM results			Interpretation of SEM results (transport process, paleoenvironment)
				Grain shape (frequency in the sample %)	Sphericity	Surface features	
LN1	SG-LN-4	IR1(n = 60)	625	>90% angular, sub angular and very angular; <10% sub rounded	low	straight grooves	glacial origin, high energy transport, potentially fluvial, potential cryogenesis/frost action
	LN-8-33	P1(n = 60)	728	60% rounded/sub rounded, 40% angular/sub angular	medium	not clearly visible	glacial origin, probable aeolian transport, pedogenesis/ frost action indicated by adhering particles
	SG-LN-5	IR2(n = 60)	769	10% very angular, over 60% angular and sub angular, the rest is sub rounded	low	subparallel linear fractures, conchoidal fractures	glacial origin, potential fluvial transport, potential frost action
	LN-H9-32B	R(n = 60)	828	Hardly visible, dominantly sub angular grains, >50%	low	not clearly visible	potential cryogenesis/frost action indicated by adhering particles
	LN-10-13	R(n = 60)	929	60% angular/sub angular, 40% sub rounded	low	not clearly visible	potential cryogenesis/frost action indicated by adhering particles
	SG-LN-6	R(n = 63)	1006	>70% angular/very angular grains in <450µm fraction; ~100% rounded/sub rounded in >450µm fraction, few sub angular	low in <450µm fraction, but high in >450µm fraction	subparallel linear fractures, conchoidal fractures, V-shaped percussion marks, parallel steps visible in <450 µm, fraction	high energy aeolian/fluvial transport, glacial origin
	LN-11-12	R(n = 60)	1040	>75% angular/sub angular, the rest sub rounded	low	possible conchoidal fractures not clearly visible	glacial origin, probable aeolian transport, potential frost action
	LN-12-12	R(n = 60)	1096	70% sub angular/angular, 30% sub rounded	low	not clearly visible	probably glacial origin and aeolian transport indicated by adhering particles
LN-13-13	IR3(n = 60)	1248	10% very angular, 50% angular/sub angular, 40% sub rounded	low	subparallel linear fractures, adhering particles	potential glacial origin and/or frost action	
LN2	SG-LN-10	P2(n = 60)	40	~ 70% angular and sub angular, 30% sub rounded. Strong alteration	low	not clearly visible	pedogenesis/ potential glacial origin /frost action indicated by adhering particles
	SG-LN-9	IR5(n = 60)	220	80% angular/sub angular grains, 20% sub rounded	low	conchoidal fractures	aeolian transport, glacial origin
Chorny Yar	SG-CY-1	Volga sand(n = 60)		50% rounded/sub-rounded, 50% angular/sub angular	medium	conchoidal fractures, subparallel linear fractures and possible V-shaped percussion mark on one grain	high energy fluvial transport, probable glacial origin

Table 3).

· Irregular unit 4 (IR4, in LN2, 42–72 cm, 4 samples; Fig. 3) appears similar to unit R in respect to most AMS parameters. F, L, and Pj values are comparable. T is oblate for all samples. κ_{\min} inclination, however, is consistently shallow <22° and κ_m is also lower than in R (Fig. 4, Supp. Table 2).

· Irregular unit 5 (IR5, in LN 2, 144–258 cm, 16 samples; Fig. 3) shows anisotropies of around 2% as well as L and F higher than in unit R. The inclination of κ_{\min} is >68° apart from three exceptions. All samples, except one, show oblate T (Fig. 4; Supp. Table 3).

Samples from the desiccation crack infills. Comparably extreme F (1.076) and L (1.022) is shown by the three samples taken from the infill material of one of the desiccation cracks observed in LN1 (approx. 7.5 m depth; Fig. 3). Also, Pj values (1.104) are higher here than in any other sample, whereas the κ_m is on average comparably low (Supp. Table 2). All three samples are oblate and show steep κ_{\min} axes (Fig. 3).

4.1.2. Comparison of the AMS groups using Jelínek and Flinn-type diagrams

Following the depth dependent separation of the 9 AMS units, their MF characteristics were compared in Jelínek and Flinn-type diagrams (Fig. 5). The grouping of the samples from the different AMS units illustrate that the R unit contains mostly oblate samples but also several prolate ones, with uniform low anisotropy. F varies more than L for most samples, some plot along the line indicating

neutral shape control (Fig. 5a and b). Two subgroups exist among the P group: P3 is, apart from two exceptions, strongly oblate with anisotropies >2% for 6 samples, whereas P1 and P2 are mostly prolate and show low anisotropies (Fig. 5c and d). Also, for the IR groups two sets of samples can be distinguished. An increase of Pj and F with increasingly oblate T, together with constant L, are seen for one set of IR samples despite strong scatter of the data. These observations are most obvious for IR5 (Fig. 5e and f). A smaller subgroup of IR samples displays prolate character, which does not coincide with an increase in Pj (Fig. 5e). It appears that the mostly prolate IR subgroup is similar to P1 and P2 as well as to a few samples from R.

4.1.3. Equal area projection analysis

The equal area projection of all 107 samples shows gravitational/flow aligned MF defined by 45% of samples, with steeply oriented κ_{\min} axes and shallow dipping κ_{\max} axes (Fig. 6a). This supports the observations from the field that the loess accumulated on a quasi-horizontal surface and suggests that MF with deviating κ_{\min} and κ_{\max} inclination signals reworking. The orientation of κ_{\max} is scattered but the κ_{\max} mean direction is NE, also indicated by the confidence ellipsoids (Fig. 6a). The alignment of the principal susceptibility axes of nearly all samples from unit R, indicates weakly oriented flow-aligned MF. Despite some scattering, a weak flow-aligned MF is also defined by the confidence ellipsoids (Fig. 6b). The alignment of the principal susceptibility axes of unit P1 and the

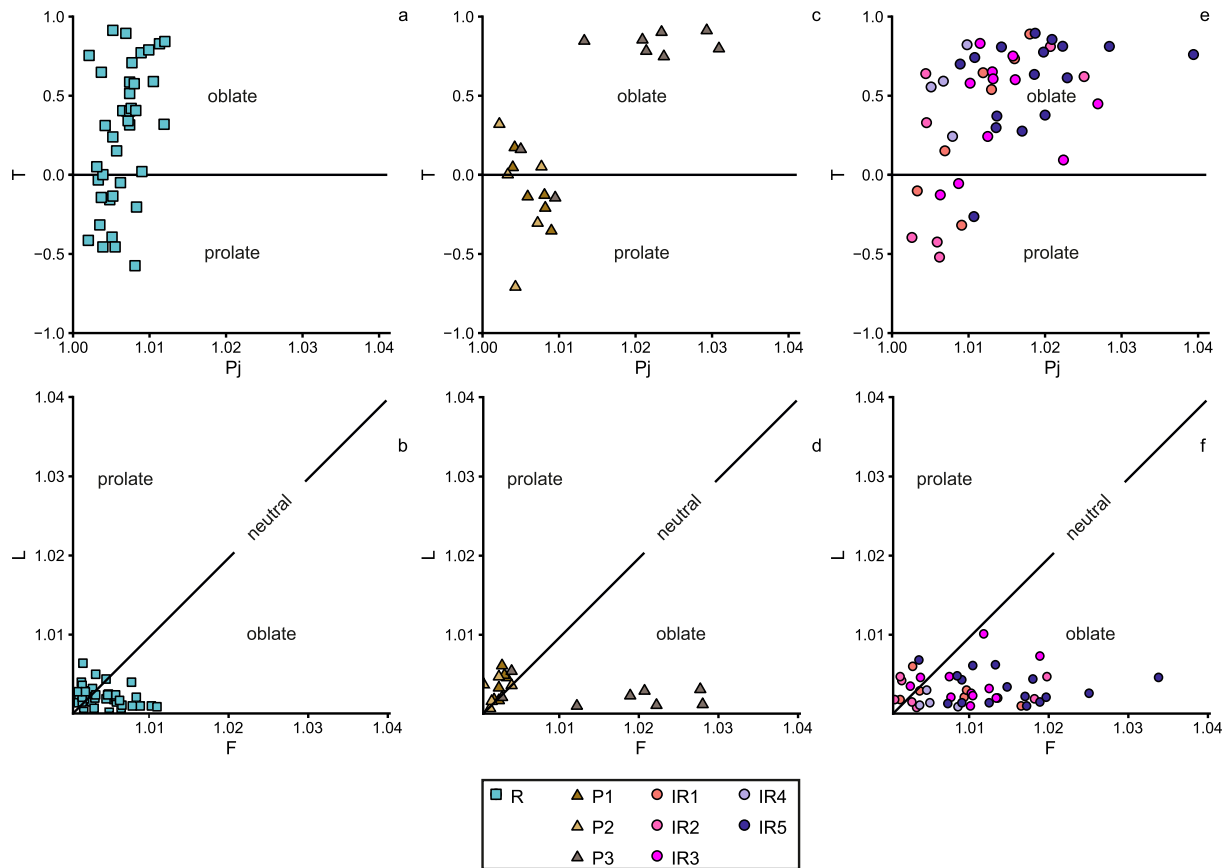


Fig. 5. The comparison of the AMS units in Jelínek (a, c, e) and Flinn-type (b, d, f) diagrams.

confidence ellipsoids show a scattered MF with a vertically oriented κ_{\max} component (Fig. 6c). The P2 unit shows a MF with mostly vertically oriented κ_{\max} and scattering alignment of κ_{\min} axes (Fig. 6d). The P3 unit shows gravitational/flow-aligned MF. The horizontal foliation plane is well-defined without a preferred orientation of κ_{\max} (Fig. 6e). IR1 displays mostly flow-aligned MF with a well-defined horizontal foliation plane and a N oriented lineation (Fig. 6f). IR2 exhibits scattered principal axes, but the confidence ellipses indicate biaxial prolate character (Fig. 6g). The principal axes and the confidence ellipse in IR3 suggest a flow-aligned fabric despite scattering (Fig. 6h). The IR4 unit shows chaotic MF (Fig. 6i). IR5 displays a well-defined gravitation/flow-aligned MF. The lineation does not show any preferred orientation, but the confidence ellipse of κ_{\max} may indicate some (Fig. 6j). The samples from the wedge infill material show horizontally foliated, gravitational/flow-aligned MF (Fig. 6k).

4.2. XRF analysis

Sr, Mg, and Ca appear depleted in units P1 and P2, while Ba and Rb are enriched compared to the R and IR units (Fig. 7). Loess from R between 8 and 9 m depth shows the opposite pattern to P1 and P2, although between 10.5 and 11.5 m depth (R) similarities to the pattern in P1 and P2 occur. The CIA values range between 58 and 76% for all measured samples, with highest values found in P2, and the lowest in loess from LN2 (IR4) (Fig. 7).

4.3. SEM image analyses

More than 70% of the scanned quartz grains in the samples are

sand-sized ($>63 \mu\text{m}$). A smaller percentage of grains ($<30\%$) are silt-sized ($<63 \mu\text{m}$). Angular grains dominate in nearly all samples making up almost 80% of the total number of grains (Table 1). Exceptions are one sample from R (1006 cm depth) and the Volga sand sample from Chorny Yar, where more than 50% of grains are partially rounded and rounded (Fig. 8a and h). Conchoidal fractures were detected in over 40% of the grains in IR2, R, IR5, and to a lesser extent in the Volga sand. A small number of these grains displays conchoidal fractures of half the length of the grain's long axis, while the majority of grains shows fractures of one quarter or less of the grain's long axis (Fig. 8b, d, l and j). Samples from IR2, R, IR3, and the Volga sand contain about 25% of all grains displaying sets of subparallel linear fractures (Fig. 8b, d, f, g, i, j and k). The length of such subparallel linear fractures ranges from 2 to 20 μm occurring in sets of 7–8 fractures per grain on average, most of which are shallow. However, some grains also display deep subparallel linear striation. The sample from unit R at 1006 cm depth is the only one for which V-shaped percussion marks and parallel steps can be found (3–5 μm in size) (Fig. 8g and i). A significant number of grains from the P1, P2, R samples have adhering particles on their surfaces, which are lattice shaped (subordinate globules).

5. Discussion

5.1. AMS units: MF and formation related processes

5.1.1. Lithological and environmental factors affecting the MF at Leninsk

A detailed magnetic investigation of Leninsk loess is provided by Költringer et al. (2020) and demonstrates that multidomain

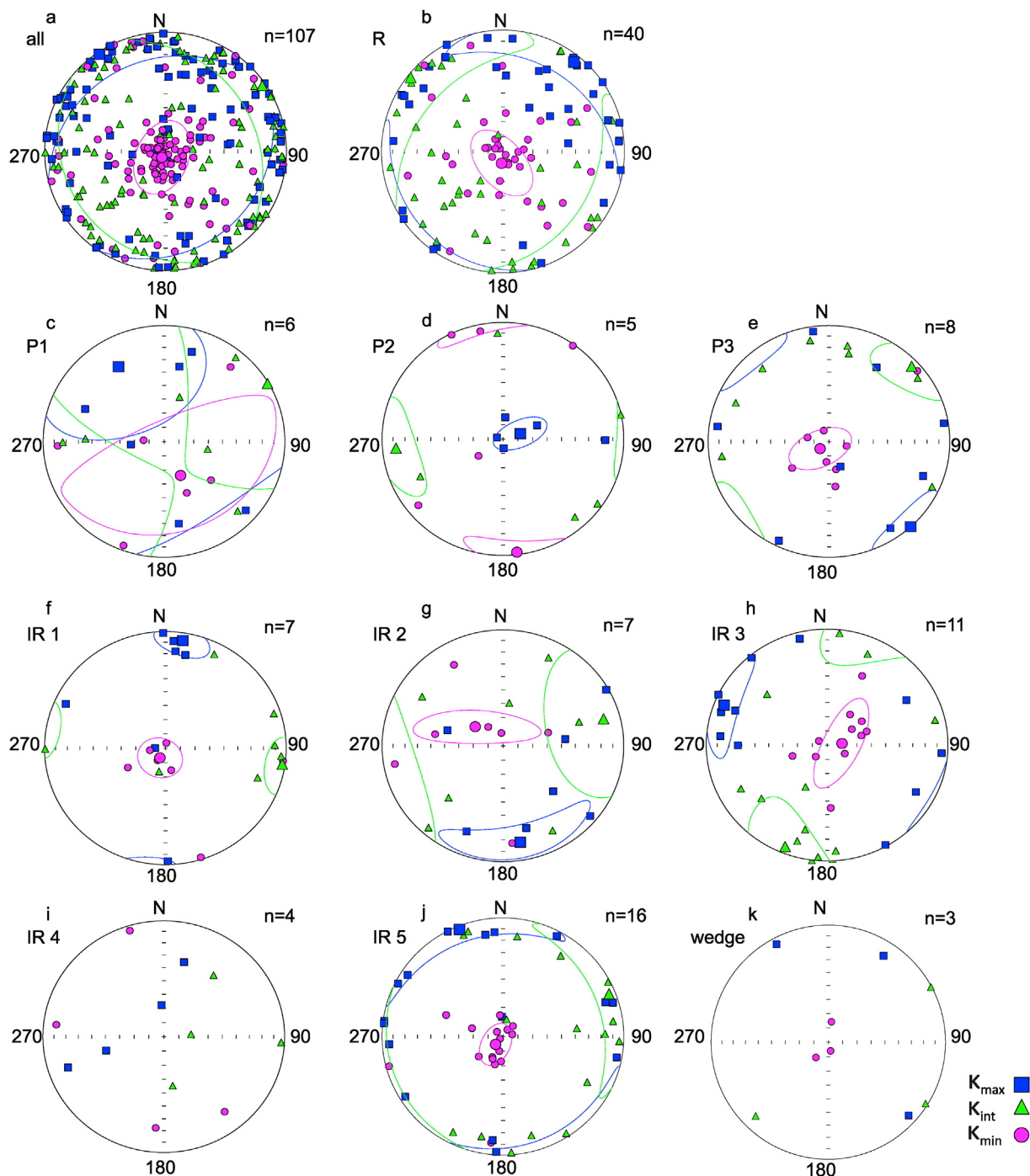


Fig. 6. Equal area projection stereoplots of AMS units (a) all, (b) R, (c) P1, (d) P2, (e) P3, (f) IR1, (g) IR2, (h) IR3, (i) IR4, (j) IR5, (k) wedge material. Mean directions of the principal axes are shown by bigger symbols of the respective colour. Confidence ellipses are displayed for each principal axis in the respective colour. (For interpretation of the references to colour in this figure legend, the reader is referred to the Web version of this article.)

magnetite is the predominant ferrimagnetic mineral. This indicates that the MF of the ferrimagnetic phase is primarily controlled by multidomain grains and, therefore, reflects the alignment of magnetic minerals that have shape preferred orientation (SPO) and intrinsically oblate character (e.g. Hrouda, 1982). As such, information about the preservation or reworking of the MF can be inferred, since crystallographic preferred lineation (CPO) does not play a role for magnetite and prolate character is not primary given. However, the role of paramagnetic minerals for the MF in loess

needs to be considered as well (e.g. Lagroix and Banerjee, 2002; Taylor and Lagroix, 2015; Bradák et al., 2018a; b). The influence of paramagnetic contributors can be expected particularly for sediments with low magnetic susceptibility (e.g., Hus, 2003). The magnetic susceptibility at Leninsk ranges between 1.63 and $1.74 \times 10^{-7} \text{ m}^3 \text{ kg}^{-1}$ and thus indicates that a considerable contribution could come from paramagnetic minerals (Költringer et al., 2020). The lack of relationship between P_j and κ_m suggests that the paramagnetic mineral fraction determines the AMS in Leninsk loess

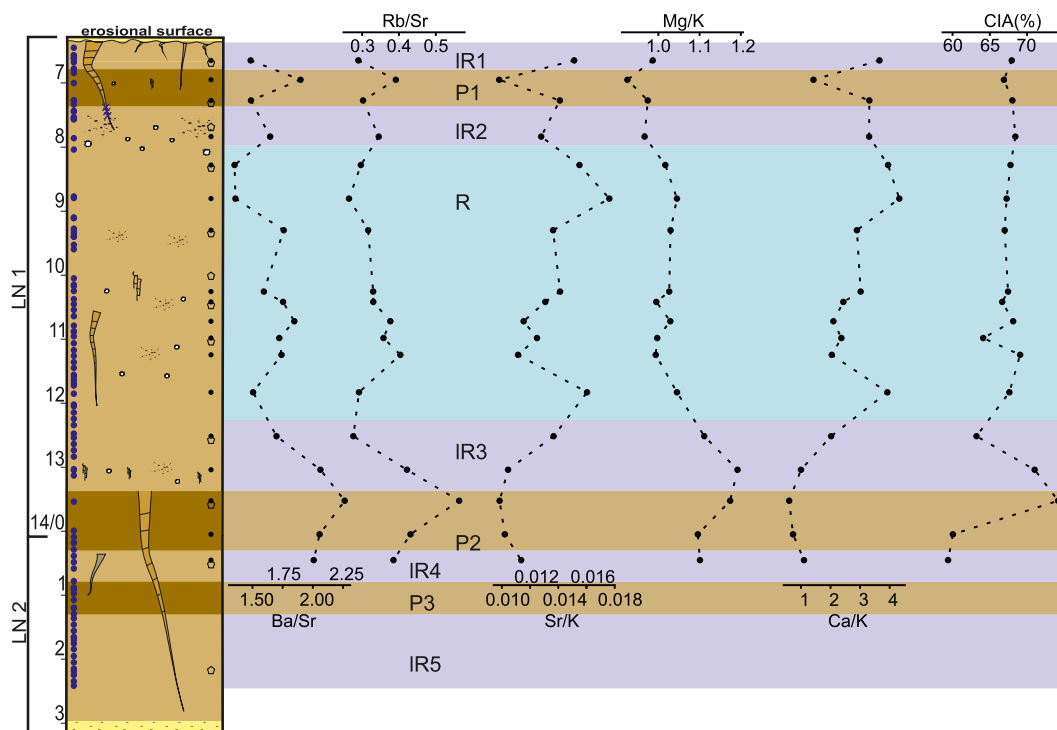


Fig. 7. Weathering indices and CIA as a function of depth. For legend see Fig. 2.

(Fig. 2g; Rochette et al., 1992; Hus, 2003; Taylor and Lagroix, 2015). The most common paramagnetic contribution in loess comes from phyllosilicates such as biotite, muscovite, chlorite and clay minerals (e.g. Taylor and Lagroix, 2015), which display intrinsically oblate AMS character (e.g. Biedermann et al., 2014). To test the influence of the paramagnetic phase on the AMS, hysteresis magnetisation parameters are used. The saturation magnetisation (M_s) of pure magnetite is $92 \text{ Am}^2\text{kg}^{-1}$ (Hunt et al., 1995), the highest measured M_s of loess at Leninsk is $0.011 \text{ Am}^2\text{kg}^{-1}$ (data from Költringer et al., 2020), which suggests that if the ferrimagnetic mineral fraction were purely magnetite, the maximum weight percentage of magnetite in samples from Leninsk would be only 0.012. This small percentage demonstrates that, even if distribution anisotropy of magnetite played a role, magnetic lineation is not caused by any ferrimagnetic particle interaction, but rather the alignment of the paramagnetic components in phyllosilicates together with the alignment of the subordinately present ferrimagnetic minerals. Similar conclusions are made by Taylor and Lagroix (2015) and Lagroix and Borradaile (2000), who calculated the minimum percentage of magnetite needed to dominate over the paramagnetic AMS contributors with 0.7 wt %. To sum up, we interpret these results to mean that the prolate character observed in the MF of the AMS units at Leninsk is related to post-depositional processes, and any lineation to primary or secondary alignment of the grains.

Along with these lithological characteristics (i.e. common appearance of paramagnetic compared to ferrimagnetic contributors and dominating multidomain ferrimagnetic grains), environmental factors might influence greater parts of the Leninsk loess profile. As such, the MF of Leninsk samples might be affected by frost action at the microscopic scale. Particle migration and translocation can occur on the thin water film associated with growing ice bodies. This movement of particles can have sorting effects (Van Vliet-Lanoë, 2010) and potentially cause lineation and imbrication in the observed MF. Freeze-thaw driven mobilization of fine grains leads to a relative coarsening and might be related to increased F.

On a larger scale, permafrost channelled ground water flow can cause the development of a lineation (Lagroix and Banerjee, 2004a). Grain alignment being indicative for freeze-thawing processes in the MF of loess has been mentioned by Hus (2003). In relation to the apparent cracks at Leninsk (Fig. 3), vertical particle translocation and random oriented displacement may also have occurred and caused chaotic MF. As such, freeze-thaw cycles, which induce stress and its release, might have caused closing and opening of the cracks.

5.1.2. "Regular" unit and forming processes

Overall, the alignment of the principal susceptibility axes (Fig. 6b) and the predominantly foliated, oblate character of R (Fig. 5a and b) indicate a primary aeolian MF (Table 2). However, post-depositional influence and the development of secondary MF is suggested by the prolate character of several samples within this unit and the varying inclination of the principal susceptibility axes (Supp. Table 3; Figs. 4 and 6b). Despite some scattering, a flow-aligned MF is indicated by the confidence ellipsoids, possibly marking an imbrication and/or the strengthening of flow-transverse/biaxial prolate fabric (Fig. 6b). R shows weak anisotropy (Figs. 4 and 5), which may reflect a relatively calm sedimentation environment, e.g. a gravitation controlled quasi permanent dust fall instead of dust storms characterized by strong winds. This scenario may explain a lack of preferred orientation of the lineation and the dominantly oblate character. A generally well defined horizontally oriented foliation plane reflects compaction without significant disturbance due to bioturbation and pedogenesis, however, the κ_{\min} of several samples is not vertically oriented suggesting reworking in some parts of the unit (Fig. 6b). There is no obvious relationship between the deviation of κ_{\min} inclination from the vertical and a prolate AMS character (Fig. 3). The relatively high Sr/K, Ca/K and Mg/K as well as low Rb/Sr, Ba/Sr suggest a low degree of alteration of silicate minerals in the upper metre of the R unit (Nesbitt et al., 1980; Reeder et al., 2006). This seems to correlate

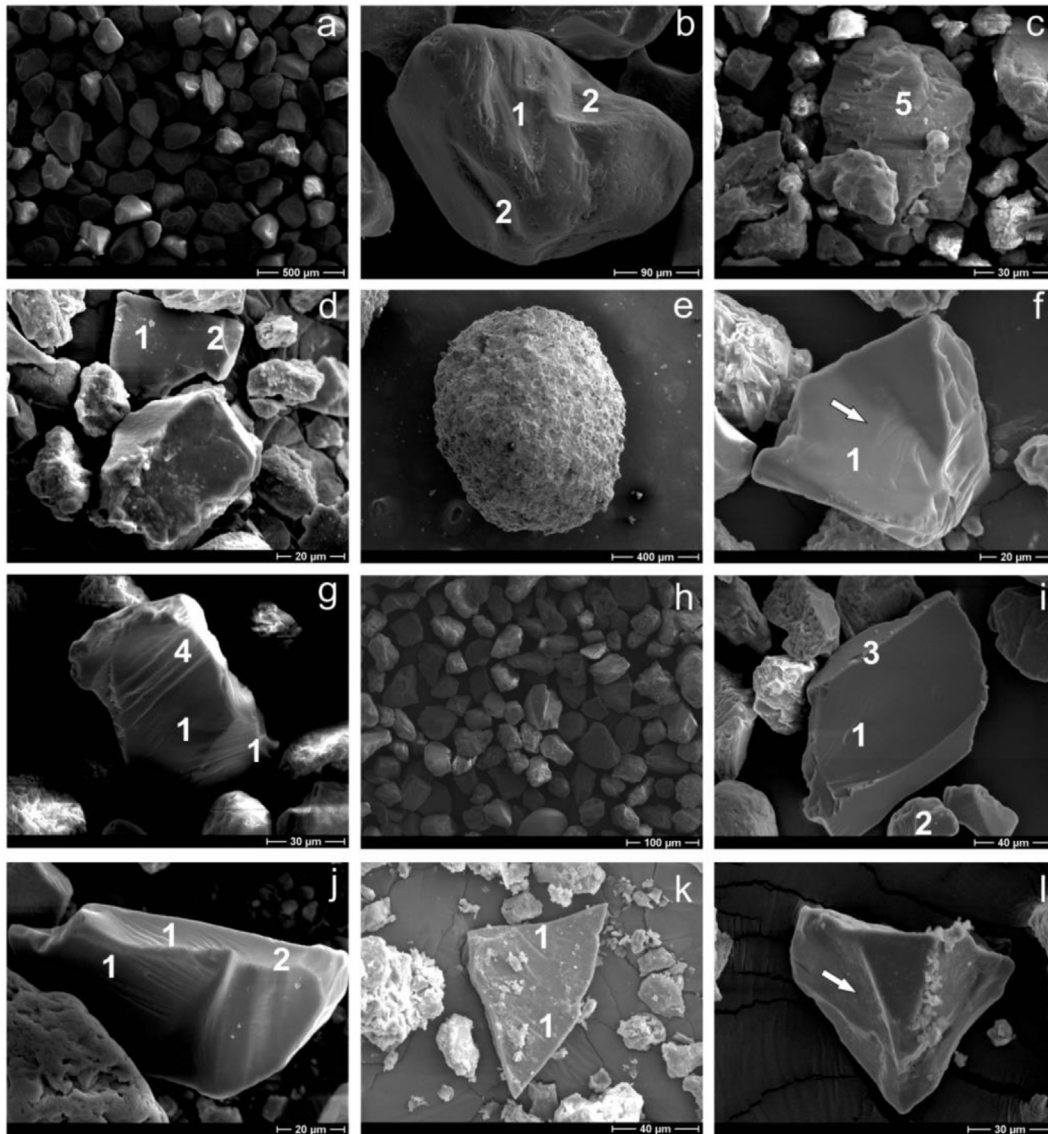


Fig. 8. SEM images of quartz grains from 7 loess samples and from 1 sand sample. The samples are arranged alphabetically according to their stratigraphic depth from top to bottom in the section. (a) Volga sand sample (bulk): overview under a smaller magnification showing dominantly sub-rounded grains (b) Volga sand sample (bulk): sub-rounded grain with shallow subparallel linear fractures (1) and either weathered conchoidal fractures or possibly edge rounding (2) (c) IR1 sample (bulk, 625 cm LN1): sub-angular grain with weathered, straight grooves (5) and adhering particles. (d) IR2 sample (bulk, 769 cm LN1): Angular grain with subparallel linear fractures (1) and conchoidal fracture (2) (e) R sample (>450 μm, 1006 cm LN1): rounded grain with strongly weathered surface (f) R sample (<450 μm, 1006 cm LN1): angular grain with fracture faces (marked with an arrow) and shallow subparallel linear fractures (1) and parallel steps in the upper part of the grain (4) (g) R sample (<450 μm, 1006 cm LN1): angular grain with subparallel linear fractures (1) and possible V-shaped percussion mark (3) are visible on the fracture face and on the edge-left side of the grain. Conchoidal fracture (2) on the smaller grain at the bottom of the image (j) R sample (<450 μm, 1006 cm LN1): angular grain with subparallel linear fractures (1) and conchoidal fracture (2) (k) IR3 sample (bulk, 1248 cm LN1): angular grain with sharp edges, adhering particles and subparallel linear fractures (1) (l) IR5 sample (bulk, 220 cm LN2): angular grain with sharp edges, partially weathered surface (marked with an arrow) and adhering particles on the right side of the grain.

with the occurrence of oblate AMS ellipsoids in R (Fig. 3). As such, the combination of geochemistry and MF data for the upper part of the R unit reflect relatively undisturbed and unweathered aeolian loess. For the middle part of R (9–11.5 m), in contrast, geochemical data indicate some weathering, which lead to the mobilization of Sr, Mg and Ca (Fig. 7). However, the depletion of these elements is not as evident as observed for the pedogenic horizons (see below). The CIA values are similar throughout the entire R unit but slightly lower for its middle part (Fig. 7). This contradicts pedogenesis and rather suggests the removal of clay minerals, for example due to fine particle migration triggered by frost action, for this middle

part. Samples of prolate character occur within this section of the R unit and raise a potential relationship between frost action and the shape of AMS ellipsoids. The low number of XRF analyses means that such a relationship can only be speculated on though. Not least, signs of cryogenesis in the middle part of unit R (Fig. 3), make cryogenic reworking of a primary aeolian MF plausible. However, prolate samples do also occur in the lower part of unit R, where no weathering is indicated by the geochemical data, no signs of pedogenesis or cryogenesis could be found in the field, and are also not indicated by magnetic susceptibility data from Költringer et al. (2020). In this part of unit R, the formation of secondary MF might

Table 2
MF criteria check for the different AMS groups and their inferred forming processes.

AMS group		MF criteria (for more information Chapter 5.1.1)						Forming process(es) of magnetic fabric	
		Foliation-controlled MF	Stereoplot analysis and the alignment of principal susceptibility axes				Shape of the susceptibility ellipsoid		
			gravitation controlled/ flow-aligned	flow-transverse / biaxial prolate	biaxial oblate	chaotic vertical	oriented lineation		
Regular AMS	R	✓	✓	✓			none	oblate and prolate	Primary aeolian, gravitational, freeze-thawing processes
Palaeosol AMS	P1					✓	✓	prolate	Bioturbation, potential cryoturbation
	P2						✓	prolate	Pedogenesis
	P3	✓	✓				✓	oblate	Primary aeolian, gravitational, weak pedogenesis
Irregular AMS	IR1	✓	✓				secondary potentially none	oblate and prolate	Cryoturbation
	IR2			✓			✓	oblate and prolate	Cryoturbation
	IR3	✓	✓	✓			secondary potentially none	oblate	Freeze-thawing and slight pedogenesis
	IR4						✓	oblate	Cryoturbation
	IR5	✓	✓				primary potentially none	oblate	Primary aeolian, gravitational
Wedge infills		✓					oblate	Secondary gravitational	

be connected to slope processes, water logging or water movement (e.g. rill wash under cold climates, Van Vliet-Lanoë, 2010).

SEM observations show evidence of ice abrasion likely to derive from the source region of the sediment. The abundant subangular grain shape together with the small conchoidal fractures and particularly the presence of adhering particles furthermore suggests aeolian transport and the alternating influence of frost action (Vos et al., 2014; Van Vliet-Lanoë, 2010). However, the formation of grain coatings of various types can also occur during pedogenesis (Mees, 2010). Nevertheless, the presence of potential cryogenic features in this part of the unit and the secondary MF along with the geochemical data, showing some element mobilization (see element ratios, Fig. 7) but no silicate/pedogenic weathering according to the CIA, support the idea of post-depositional cryogenesis in loess. V-shaped percussion marks, the result of grain collision, and the angular and partly rounded shape, suggest high transportation energy via wind or water (Mahaney, 2002).

5.1.3. Pedogenic AMS unit and the development of MF in palaeosols

The scattering of κ_{\max} and κ_{int} axes, some vertically oriented κ_{\max} , and the abundance of prolate shape ellipsoids, indicate reworking for unit P1 (e.g. Matasova et al., 2001; Bradák et al., 2011, Figs. 5 and 6c, Table 2). The decrease in F can be indicative for soil formation as described by Zhu et al. (2004). The stronger lineation in combination with the presence of wedge-like features suggests cryogenesis, which may have affected P1 (Fig. 3). Such processes could be reflected in the scattered data and occurrence of vertically oriented κ_{\max} . The weathering indices show relative depletion of highly mobile elements in weathering environments (Sr, Ca, Mg). In contrast, a CIA of around 67% is not indicative for pedogenesis (Fig. 7), but cryogenesis might have preconditioned the removal of clay minerals and led to freeze-thaw related particle migration, similar to the translocation of clay during slow percolation (Dasog et al., 1987). Weathering processes are also indicated by the presence of adhering particles as revealed by the SEM images. However, the common rounded and sparse sub-angular shape indicates an aeolian origin of the parent material.

Observations from P2 match the findings of Zhu et al. (2004), who suggested that low Pj and F coincide with pedogenesis. In line

with this result, the parent material (pm P2), in which P2 developed, shows higher F and Pj. Similar to that seen in P1, L is comparably high in relation to F. Considering the vertical component of κ_{\max} , its prolate character, together with the indication for weathering from the element ratios, the high CIA and the alteration of grain surfaces (SEM), P2 appears to be affected by pedogenesis, most profoundly in its upper part (Fig. 5c and d, 6d and 7, Table 2). The less distinct sign of chemical weathering in the lower section of P2 might be in relation to frost action and the connected potential removal of clay minerals. This is suggested by the presence of distinct cracks/wedges in this part of the pedogenic unit.

P3 contains several samples of foliation controlled primary, aeolian MF (Fig. 6e). The lack of a preferred orientation and the predominately oblate character, might indicate gravitational affected MF but could also reflect the dominance of paramagnetic matrix minerals (Fig. 5c). P3 also differs from P1 and P2 by showing significantly higher F and Pj, even compared to the pristine loess layer R (Figs. 3 and 5). Similar to Lagroix and Banerjee (2004b), who also observed increasing F and Pj for palaeosols, our results contrast with the observation from some loess studies that Pj is systematically lower in palaeosols compared to undisturbed loess (Hus, 2003; Matasova and Kazansky, 2004). In both cases (Alaskan loess; Lagroix and Banerjee, 2004b; and LVL; Költringer et al., 2020) the pedogenic horizons are weakly developed, which may explain why in such cases Pj is not necessarily lower than it is for loess. P3 does not seem to have experienced profound reworking, which agrees with findings from Költringer et al. (2020) that weak pedogenesis occurring in the Lower Volga loess sections has little influence on its magnetic properties.

5.1.4. "Irregular" unit

Samples from IR1 show flow-aligned MF with N–S oriented lineation (Figs. 3 and 6f). No pedogenesis is indicated, neither from geochemical nor SEM data. However, L and F are higher than for the regular loess, and a vertical component of κ_{\max} as well as prolate character of one sample indicate some post-depositional influence on the MF (Figs. 4 and 6f). Post depositional disturbance becomes also clear from distinct cracks in the unit. For this reason, the unit seems to have been reworked by cryogenesis, which also might

have caused the flow-aligned MF. The abundant angular grain outline and the straight grooves on the grain surfaces are known from glacial environments and rather connected to the grains' provenance than in situ frost action (Mahaney, 2002).

The secondary MF of IR2 shows evidence for reworking (Fig. 6g). Samples with strong F, $T > 0$, and high Pj stand in contrast to samples with prolate character, weak F, and low Pj (Fig. 5e and f). The latter group of characteristic properties are similar to those of P1 and P2, and several R samples (Figs. 3 and 5). The partly strong F and pronounced L suggest the occurrence of frost action. Frost action may also be reflected by the biaxial prolate MF (Fig. 6g; Lagroix and Banerjee, 2004a). Considering the presence of cracks in this part of the section and the lack of evidence for pedogenesis, this suggests reworking by cryogenic processes (Fig. 3). IR2 contains grains with subparallel linear fractures, diagnostic marks of ice abrasion (Fig. 8d; Table 1) (Strand and Immonen, 2010). As such, these features are likely inherited from the loess source material as the influence of in-situ cryogenesis might not be as forceful on the grains without causing significant redeposition of the loess. The common sub-angular and the sparse rounded grain shape are evidence of fluvial transport (Vos et al., 2014), so that river transport from a glacial outwash plane and final aeolian deposition seem likely.

IR3 indicates the occurrence of some form of reworking and/or redeposition, which lead to the formation of stronger F, a pronounced L, and the increase of Pj compared to the undisturbed loess of the R unit (Figs. 3 and 5e and f). Considering the entire sample population of the IR3 unit, the alignment of the principal susceptibility axes and confidence ellipses show biaxial prolate MF, which also suggests reworking resulting in the disturbance of the primary MF (Fig. 6h). A preferred WNW-ESE orientation is indicated by the declination of κ_{\max} . Költringer et al. (2020) suggest that prominent frequency dependent magnetic susceptibility features in the upper part of IR3 (~12.4 m) may be linked to the presence of permafrost and the accumulation of superparamagnetic minerals due to its low permeability. As such, the development of lineation and foliation in this unit can be related to such forms of cryogenesis (e.g. removal of fine particles and channelled water movement), and subparallel striation on grains shows the influence of frost and glacial action. Apart from these secondary features, observed in the upper part of IR3, several samples show primary MF too (Fig. 6h). The observed preferred orientation, however, is more likely to reflect a secondary than primary lineation, since it is defined by samples with non-horizontal κ_{\min} . Weathering indices and the CIA from the two analysed samples from IR3 indicate increasing alteration with depth, suggesting that this lower part of the unit, adjacent to the underlying pedogenic layer, could have experienced weak pedogenesis as well, which did probably not severely affect its MF (Fig. 7, Table 2).

The IR4 unit shows chaotic MF (Fig. 6i). Even though this observed MF indicates post-depositional reworking, the low number of samples from this unit makes it hard to evaluate. Weak chemical weathering is suggested from the element ratios, where in contrast the CIA is low. Just as for the lower part of unit P2, this might be related to the presence of cracks/wedges and signal cryogenic reworking (Fig. 3).

IR5 was grouped due to high Pj and strong development of F and L (Figs. 3 and 4). The unit is described by well-defined gravitation (/flow)-aligned fabric with oblate character (Fig. 6j). The lineation of these samples does not show any significant orientation, although the confidence ellipse of κ_{\max} may indicate some. Also, the comparably high degree of anisotropy, L and F could point towards an alignment along a preferred orientation within the bedding plane. The only signs that point towards post-depositional reworking are one sample with vertical κ_{\max} and one prolate

sample.

Comparing the equal area stereoplots of all IR units allows the description of a hypothetical alteration path. IR5 shows properties of well-defined horizontal foliation and a potential aligned lineation, indicating little reworking. The scattered MF of IR3 and stronger L and F in IR1 indicate increased alteration. More profound reworking is indicated for IR4 with its chaotic MF, as well as for IR2, for which also the confidence ellipses reflect biaxial prolate character.

5.1.5. Wedge infill material

Clear bedding of the wedge infill material was observed in the field and also in the AMS. This distinct alignment of grains coupled with compactional loading might be the reason for the very strong F. Mechanical stresses might have occurred due to frost heave. The differential frost heave capabilities of the coarser grained wedge infill material and the finer, pedogenic affected loess (AMS groups IR1, P1, IR2) might explain the differences in F. The high Pj (≥ 1.1) shown by the three samples together with the positive T of >0.5 indicate a possible intensification of foliation, perhaps through compaction perpendicular to the primary foliation (bedding) plane (Supp. Table 2). In addition to the F-controlled susceptibility ellipsoid, the orientation of the principal axes is the same as for aeolian MF and does not show signs of disturbance as far as the limited number of samples allows such inference (Fig. 6k). Overall, the wedge infill may represent primary aeolian material that developed a secondary foliation and more distinct lineation (Table 2).

5.1.6. Preserved primary aeolian MF

Samples reflecting primary MF could be identified for several units (Table 2). As explained in 3.1.1, a set of criteria is applied to test whether this primary MF is indeed aeolian as suggested by previous studies (e.g. Lebedeva et al., 2018; Költringer et al., 2020). 45 samples from the loess passed the criteria for aeolian MF on a sub-horizontal surface, according to the orientation of their principal susceptibility axes from the equal area stereoplot analyses (a horizontal foliation with inclination $\kappa_{\min} > 70^\circ$; Fig. 9a). Among these, there are eight samples of prolate character (Supp. Table 3). The control of the AMS in Leninsk loess by paramagnetic contributors suggests a relationship between post-depositional reworking and prolate character due to the intrinsically oblate character of the AMS contributors (Fig. 2g; 5.1.1). As such, only samples with oblate character (37) are further isolated (Fig. 9b). The testing for statistical significance shows that all of these 37 samples have significant magnetic foliation ($F_{23} > 10^\circ$) and 24 samples show also significant magnetic lineation in addition. Out of these 24 samples, the AMS of one sample is equally controlled by F and L and for this reason removed together with all statistically insignificant samples (Supp. Table 3). This process leaves 23 samples for final consideration of palaeowind reconstruction (Fig. 9c).

5.2. Loess formation and transport

Loess from Leninsk contains many grains with sharp edges, dominantly angular morphology, medium to high relief and conchoidal fractures. Few grains display V-shaped percussion marks, parallel steps and subparallel linear striations. While the common characteristics of aeolian transport are present (Mahaney, 2002 and references therein), signs of glacial erosion and fluvial transport also exist in some samples. In comparison, the fluvial Volga sand consists of rounded and subangular grains, showing subparallel linear striations and subordinate conchoidal fractures. The close similarity between Volga sand and loess suggests fluvial transport from a probable glacial source, as indicated by glacial grinding features for both sediments, and an additional aeolian

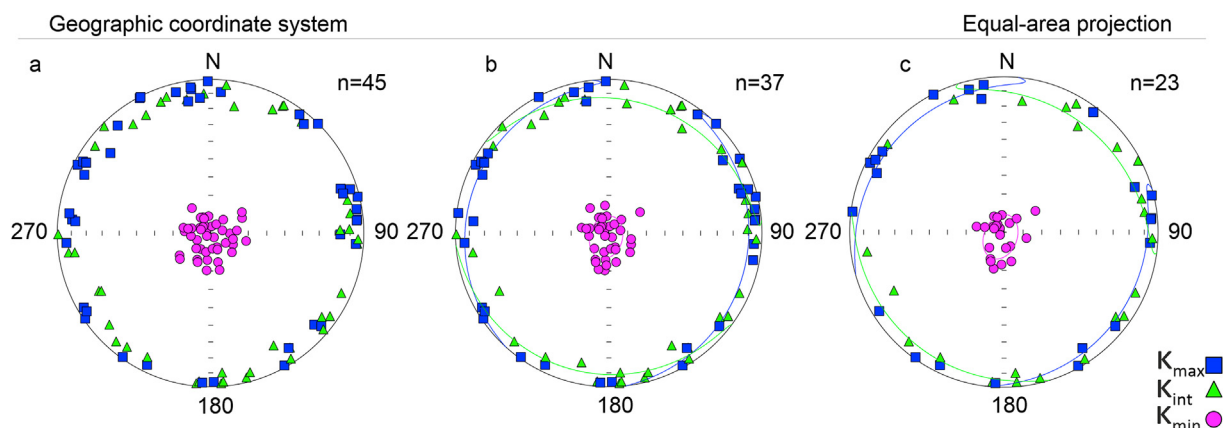


Fig. 9. Equal area stereoplots of (a) loess specimens from all LN units showing primary aeolian MF, (b) specimens with aeolian MF from all units without those showing prolate character, (c) statistically significant, oblate aeolian MF from all units.

near source transport step for final deposition of the loess (indicated by conchoidal fractures). As such, this seems consistent with the silt/sand material of LVL originating from the north of the East European Plain (EEP), where the Fennoscandian Ice Sheet produced large amounts of fine grained, silt sized till material during the last glaciation, during which the LVL accumulated (Fig. 1). This glacial material formed proglacial outwash deposits that were transported south by river systems and ultimately into the Volga River. In turn, this Volga alluvium is likely to be the sedimentary source for the aeolian transported LVL deposits. The potential impact of cryogenesis on the mechanical surface microtexture of grains is indicated by the difference in grain outline between Volga sand and LVL. The higher degree of angularity and sharp edges of LVL grains could be caused by cryogenic post-depositional grain breaking without edge rounding, similar to what is known from glacial crushing (e.g. Helland and Holmes, 1997). Also, the adhering particles on LVL grains in some horizons suggest cryogenic processes similar to those in glacial environments, where the formation of abrasion fatigue facilitates small particles to attach to the surface of the grains (Mahaney, 2002). The same can also be diagnostic for aeolian transport though, making the adhering particles also a sign for a final-stage aeolian transportation. As such, while the results here are consistent with an ice sheet origin in the EEP for the LVL, with transport to the Northern Caspian lowland via the Volga River, this remains to be confirmed by further provenance study.

5.3. Reconstructed Late Pleistocene palaeowind direction

The identified primary aeolian MF with recorded transport direction can be found mostly in the AMS units R (8 samples), P3 (3 samples), IR3 (3 samples) and IR5 (8 samples). In contrast, the units IR1 and IR2 contain only one sample that is eligible for palaeowind reconstructions, and in IR4 and P1 and P2 there are none. This analysis matches the discussion of the post-depositional reworking of the MF for each unit well (5.1). Since most samples that are eligible for palaeowind analyses occur within the same and consecutive units, their MF can be considered collectively for palaeowind reconstruction even though a denser sampling resolution for specific units would have been beneficial. For the two comparably isolated samples (by depth), it should be kept in mind that only a short snapshot in time is represented by their MF (Supp. Table 3) and the results may not be representative of the wider unit.

The mean direction of κ_{\max} together with the orientation of the confidence ellipses in the flow-aligned MF indicates a generally dominant NW-SE or SE-NW wind direction during loess deposition

at Leninsk (Fig. 9c). A second set of samples with aligned κ_{\max} defines a dominant E-W or W-E wind direction. These two main directions are indicated also by the stereoplots of aeolian MF prior to the isolation of oblate and statistically significant samples (Fig. 9a and b). However, despite these apparent prevailing wind directions, the scatter of κ_{\max} might indicate several influences on the wind direction and its potential change with time, if the lack of preferred lineation is not an effect of the dominating paramagnetic minerals on the AMS. It is also possible to infer relative changes in wind speed from the AMS data. A higher degree of alignment and anisotropy in combination (Supp. Table 3, L and Pj parameters) is observed at the base of Leninsk (Fig. 3, IR5, P3, IR3) and serves as a sign for stronger winds (Bradák et al., 2018a) at this time, compared to later loess accumulation. Finally, as discussed in section 5.1, loess deposits at the base of the section (IR5, P3) remained generally undisturbed and weak pedogenesis did not cause significant reworking of the sediments despite the presence of pedogenic unit P3. A first age estimate of the Leninsk section based on optically stimulated luminescence ages (Kurbanov et al., 2020 and further unpublished ages currently in preparation for publication) allows the attribution of Leninsk loess to MIS 5 b to 3 (~85–25 ka) (Költringer et al., 2020). The relatively coarse-grained character of Leninsk loess (coarse silt, fine sand) suggests a rather short distance of aeolian transport before deposition (Lebedeva et al., 2018). As such, in addition to larger scale regional winds, near surface winds, which can vary locally and are probably influenced by local topography and conditions, might be recorded in the MF.

For comparison to the AMS-derived palaeowinds, hourly wind data from the past 30 years measured at 10 m and 100 m height during December, January, February (winter) and June, July, August (summer) were analysed for the northern Black Sea–Caspian Sea region as well as for the ERA5 reanalysis' closest grid point to Leninsk. Average wind speeds during winter are significantly higher than during summer (Supp. Fig. 1a, b, e, f, g, h, 2, and 3) and predominantly blow from the WSW and ESE at Leninsk (Supp. Fig. 1c, d, e, f, g, and h). By contrast, dominant summer winds tend to blow from the NE and NW. Winds at 100 m height show clearly stronger speeds than at 10 m but no differences in wind direction are apparent (Supp. Fig. 1c, d, e, f, g, and h). Higher wind speeds during winter than summer are also reported by Ibrayev et al. (2010), while their observations of modern winter and summer wind directions, similar to those discussed by Rodionov (2003), demonstrate prevailing southerlies during winter and northerlies during summer. However, the observations above for Leninsk show some differences to this pattern, particularly in

winter when a more W-E component stands out (Supp. Fig. 1). When modern wind patterns for winter are plotted over a wider area, the influence of local topography on wind direction at Leninsk becomes clear (Supp. Fig. 2). The valleys of the Volga and Don river, and the Manych depression are characterized by lower wind speeds. The Yergeni uplands (the topographic high between the depressions of Manych and the Northern Caspian lowland) and the Volga uplands to the north of Leninsk, seem to deflect wind directions and change wind speeds over a wide area, including around the Leninsk site. This topographic control on winds is not visible for summer winds, probably due to the generally lower wind speeds (Supp. Fig. 3). Topographic highs in the lowland, however, are identifiable due to relatively higher wind speeds in both summer and winter. This of course is different for very mountainous regions with high relief as can be seen e.g. for the Caucasus, the mountain belt between the Caspian Sea and the Black Sea (Supp. Figs. 2 and 3). As such, while the modern observations over the wider area suggest seasonally alternating dominant N–S and S–N winds, topographic conditions modify this wider pattern so that winds at Leninsk have a stronger zonal component (W–E and E–W). There is a strong apparent similarity between present and our reconstructed Late Pleistocene dominant wind directions at Leninsk. The modern wind regime in winter shows a strong west to east component (Supp. Fig. 1), which seems to be also one of the dominant wind directions in the AMS data (Fig. 9c). This matches observations of Nawrocki et al. (2018) for Ukrainian Black Sea loess, where the reconstructed NW–SE palaeowind directions also coincide with present-day winds. On a wider regional scale, palaeowind studies from Siberian loess fit these observations as well and suggest W–E as the dominant Pleistocene and modern wind direction (Matasova et al., 2001). The stronger winds in modern wintertime and the evidence for variable strong winds from the AMS data combined with the presence of cryogenic features (Fig. 3), further suggest a modern winter-time type wind regime dominating during loess deposition at Leninsk. Loess accumulation at Leninsk probably coincided with late MIS 5 to MIS 3 (~85–25 ka), although the age model at present is preliminary (Költringer et al., 2020). Globally, MIS 4 was cooler and with increased ice volume, compared to MIS 5 and MIS 3 (Lisiecki and Raymo, 2005). On the whole, this seems to apply also for the southern EEP/Black Sea–Caspian Sea region. Liang et al. (2016) infer decreasing temperatures and increasing wind intensities for the transition from MIS 5 towards MIS 4 from loess in the Azov Sea region. Költringer et al. (2020) demonstrated that the climate became comparably milder and more humid from MIS 4 towards MIS 3 in the Lower Volga region (LVR) but was still overall cool. Our findings here agree with arguments presented by Költringer et al. (2020), by showing that P2 (~MIS 5a) and P1 (MIS 3) experienced detectable reworking in association with pedogenesis during phases of warmer and/or more humid climate. However, signs of frost action and active layer processes (e.g. solifluction) indicate generally cool but less stable conditions during MIS 5 and MIS 3 than during MIS 4, with potential higher temperature and humidity. This may imply that over the Caspian Sea Basin region, a modern wintertime pattern, with a strong west to east wind component at Leninsk, was dominant during late MIS 5, MIS 4 and 3.

Thus, local westerly flow tends to occur at Leninsk during the Late Pleistocene, but besides the westerly wind direction also a NW–SE/SE–NW wind component is suggested by the preserved aeolian MF. The inference of wind directions is further complicated by some scattering of κ_{\max} . Despite this, even though winds at Leninsk are influenced by local topography, they are, however, primarily a function of the influence of the wider scale patterns. The last glacial Fennoscandian Ice Sheet itself played a significant role in the general circulation during the Late Pleistocene by forcing the

Northern Hemisphere westerlies further south (Chapman and Maslin, 1999). Modelled winds for the last glacial maximum show prevailing north–westerlies (36% of the time) and westerlies (22% of the time) in the Northern Caspian lowland (Schaffernicht et al., 2019). These model predictions are consistent with AMS-derived palaeowind reconstructions for Leninsk (Fig. 9) and leads to the reconstructed palaeowind pattern for the Late Pleistocene shown in Fig. 10. It is inferred that prevailing westerlies and north–westerlies dominated south of the Fennoscandian Ice Sheet (Fig. 1), forcing the local southerly winter winds in the Caspian Sea region further south (Fig. 10). The local topography leads to a decrease of wind-speed in valleys and deflects the wind direction along large river valleys such as the Volga valley and the Manych depression (Fig. 10). Furthermore, wind intensity appears to have been strongest at Leninsk during the early part of loess deposition associated with late MIS 5 and MIS 4, with less intense flow under MIS 3 conditions recorded higher up in the sequence (Fig. 3, L and Pj parameters). Again, this result is consistent with stronger winds in modern wintertime at the site and over the wider region (Supp. Figs. 1, 2). As suggested by Költringer et al. (2020) and inferred also from palaeosol–loess records in the neighbouring Azov Sea region, MIS 4 was the coldest phase of the last glaciation in the area (Liang et al., 2016) and wind intensities were generally the strongest (Novothy et al., 2011).

Today the wind regime in the Caspian Sea region is controlled by several factors, when considering wider forcing. The North Atlantic oscillation (NAO) shows a strong linkage to winter precipitation at the Caspian coast (Branston and Livezey, 1987; Molavi-Arabshahi et al., 2016). Positive phases (NAO (+)) associated with strong mid-latitude westerlies over the North Atlantic and the North Pacific at 700 hPa geopotential level during winter are connected with a decline in Caspian Sea level, driven by lower winter precipitation over central-southern Europe and the Caspian Sea region (Rodionov, 2003). The NAO (+) tends to also decrease temperatures in the Caspian Sea region by bringing cold Arctic air with north-westerly winds (Rodionov, 2003). Loess accumulation in the LVR is associated with cold climate, low precipitation and low Caspian sea level stand (e.g. Költringer et al., 2020). While NAO (+) atmospheric conditions appear similar to those during the cold Atelian regression of the Caspian Sea, a major control on the Caspian Sea level stand in the Late Pleistocene, is seen in river discharge from the EEP and Siberian Plain (e.g. Kislov et al., 2014; Panin and Matlakhova, 2015). The northern EEP ought to receive more precipitation during phases of NAO (+) due to the northward shift of major storm tracks transporting warmth and moisture from the North Atlantic, which would suggest an increased river input into the Caspian Sea. However, during the Late Pleistocene, most of this additional precipitation would occur as snow and get stored in the northern EEP without simultaneously causing increased river discharge. Also, in the Pleistocene, rivers draining the Siberian Plain used to play a major role, where at present the Siberian high, a supra-continental high pressure atmospheric system, causes extremely cold and dry conditions during winter (D'Arrigo et al., 2005). Presuming that modern-day winter atmospheric conditions over Eurasia are comparable to those in the Late Pleistocene, this means no increased river discharge from the Siberian Plain into the Caspian Sea. Hence, although likely less pronounced, modern NAO (+) situations might represent a similar dynamic than during the loess deposition in the LVR. More generally, the cold conditions in the Caspian Sea region during times of loess accumulation, when the north of the EEP was glaciated, match well with the finding that enhanced modern snow cover on the Russian Plain (lower temperatures) is associated with cooler temperatures in the Caspian Sea region (Molavi-Arabshahi et al., 2016). However, another influence on the climate in the Caspian is the North Sea–Caspian

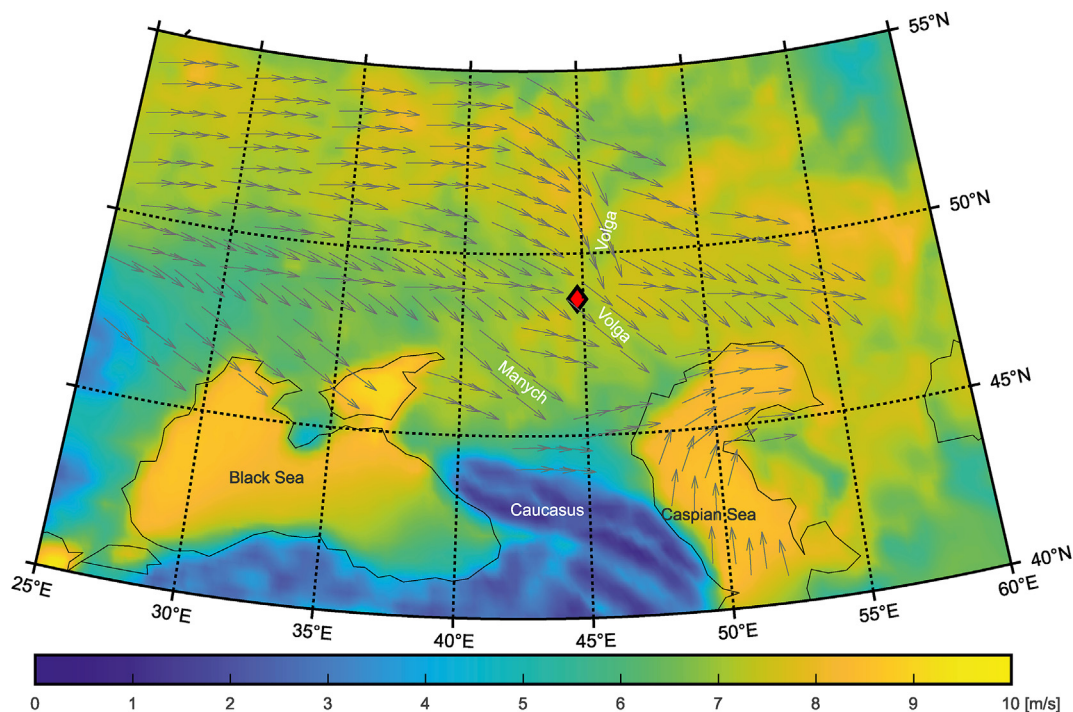


Fig. 10. Map of the southern EEP/Black Sea- Caspian Sea region showing reconstructed prevailing wind speeds and wind directions in the Late Pleistocene according to the findings of this study (LVR) and Nawrocki et al. (2018) (Ukrainian Black Sea region) in reconciliation with the model prediction of Schaffernicht et al. (2019). The red diamond marks the location of Leninsk. The potential influence of the topography on wind speed and wind directions is considered. (For interpretation of the references to colour in this figure legend, the reader is referred to the Web version of this article.)

pattern (NCP) at 500 hPa geopotential level. Kutiel and Benaroch (2002) demonstrated that the NCP occurs most frequently during winter and is negative for most of the year. These NCP(−) episodes are linked with strengthened south-westerly winds in the Black Sea- Caspian Sea region (a direction suggested by a few AMS samples), lowering precipitation but increasing temperatures, which would speak for a stronger NCP(−) control, potentially during interstadials with warmer climate.

Despite many potential similarities between palaeo- and modern climate conditions, the comparison of these findings with wider scale patterns and controls on winds during the last glacial period is limited by a) the low AMS sample resolution at Leninsk b) the strong topographic control over winds at Leninsk and c) the uncertain relationship between modelled or reconstructed wind directions from other proxies, such as grain size and provenance analyses, and winds associated with dust transport (e.g. requiring a certain strength, and possibly being gusty).

To test whether the short phases of warmer/more humid climate in the LVR, marked by signs of pedogenesis in the loess sequences (Költringer et al., 2020), also occur with changes in wind speed and/or directions, similar to the seasonal changes between winter and summer winds at modern days, the AMS of samples from loess and pedogenic units are directly compared. No systematic differences in any of the AMS parameters (e.g. L and Pj as signs for wind strengths) or in the orientation of the principal susceptibilities can be observed between loess and pedogenically affected samples (Supp. Table 3). This result suggests that the climatic shifts during phases of pedogenesis probably did not occur with concurrent significant changes in wind direction or strength. As known from the present-day observations, several global atmospheric circulation patterns can have an influence on the climate in the Caspian Sea region. While these different teleconnections can drive precipitation and temperature differently, the resultant

prevailing wind directions might be similar, as for example in the case of NAO (+) and NCP(−), which both cause dominantly (N/S-) westerly flow in the Black Sea- Caspian Sea area, but change temperature in opposite ways.

6. Conclusions

Our study presents a novel combination of detailed AMS analyses, SEM and geochemical proxies, which sheds new light on the loess MF reworking in cold climates and the responsible processes. It addresses questions about origin, formation and alteration of Lower Volga Loess (LVL) and its role in the reconstruction of prevailing wind directions and shows that the loess at Leninsk:

- is aeolian, likely produced by glacial-grinding and transported by multi-step fluvial and aeolian transport.
- experienced post-depositional reworking (cryogenesis, pedogenesis) for several horizons, revealing palaeoenvironmental conditions.
- allows the reconstruction of palaeowind directions from preserved primary aeolian MF.

The presence of loess grains with angular morphology and conchoidal fractures, besides those with V-shaped percussion marks, parallel steps and subparallel linear striations, indicate a glacial source for the ultimately wind-blown material. The great similarity between LVL and Volga sand samples raises the importance of river transport for dust from production areas to depositor centres. The combination of this evidence and the geographical and temporal context suggest proglacial outwash deposits of the Fennoscandian Ice Sheet in the East European Plain are the source material for LVL, which was subsequently transported to the south of Russia via rivers (Volga) and blown by wind into the final loess

deposits.

The imprint of frost action on the MF of loess and its potential for overwriting the primary aeolian MF, as found at Leninsk, seems to be a rather rare phenomenon, with similar observations only reported from Alaskan loess (Lagroix and Banerjee, 2004a) and supposedly from the Hungarian Paks section (Bradák et al., 2019). The new results of our study complement these earlier findings and strongly suggest that scattered and biaxial prolate MF, with possible imbrication, indicates freeze-thawing related particle migration in loess in cold environments. Frost action, disturbing the primary MF, increased during MIS 4 and confirms this to have been a cold period in the region. Warming coincident with the beginning of MIS 3 is suggested by pedogenesis, however, horizons are clearly still affected by cryogenic reworking. This further suggests that MIS 3 pedogenic horizons developed in a generally cold but more variable and more humid climate regime. The disturbed MF of the weak pedogenic horizons at Leninsk indicates the influence of soil formation, in agreement with the findings of Költringer et al. (2020) and supporting their inferences of pedogenesis (i.e. based on temperature dependent magnetic susceptibility data) despite the indistinct evidence from frequency dependent magnetic susceptibility.

This suggested climate evolution is also supported by the palaeowind reconstructions, indicating stronger winds associated with cooler temperatures during early MIS 4. The overall prevailing wind direction during the Late Pleistocene at Leninsk was variable but dominantly W-E and NW-SE (Fig. 10), although a denser sampling resolution in depth would be beneficial to disentangle the predominance and variation of wind directions over time. Reconstructed palaeowinds at Leninsk are similar to the present-day situation but the presence of several factors such as locally influenced winds plus wider scale atmospheric circulation patterns complicate interpretations of wider forcing.

Author statement

Chiara Költringer: Conceptualization; Data curation; Methodology; Formal analysis; Visualization; Writing – original draft. Balázs Bradák: Conceptualization; Data curation; Formal analysis; Supervision; Writing – original draft. Thomas Stevens: Conceptualization; Supervision, Writing – review & editing. Bjarne Almquist: Supervision; Writing – review & editing. Adriano Banak: Methodology; Formal analysis. Martin Lindner: Methodology; Formal analysis; Visualization. Redzhep Kurbanov: Conceptualization; Data curation. Ian Snowball: Writing – review & editing

Declaration of competing interest

The authors declare that they have no known competing financial interests or personal relationships that could have appeared to influence the work reported in this paper.

Acknowledgements

We are grateful to Friedrich Xinger for offering the facilities for XRF analyses at Salzburg University. Thanks go also to Christoffer Hallgren from Uppsala University for his support with the wind data and the helpful discussions. Natalia Taratunina, Vladimir Belyaev, Yunus Baykal, Gábor Újvári, Jan-Pieter Buylaert and Warren Thompson are thanked for their help during field work and sample taking. B. Bradák acknowledges the financial support of project BU235P18 (Junta de Castilla y León, Spain) and the European Regional Development Fund (ERDF), project PID2019-108753 GB-C21/AECI/10.13039/501100011033 and project PID2019-105796 GB-100/AECI/10.13039/501100011033 of the

Agencia Estatal de Investigación. R. Kurbanov acknowledges the Russian Science Foundation project 19-77-10077. The Swedish Research Council is gratefully acknowledged for funding to T. Stevens for part of this project (2017–03888).

Appendix A. Supplementary data

Supplementary data to this article can be found online at <https://doi.org/10.1016/j.quascirev.2021.107057>.

References

- Arkhipov, S.A., Ehlers, J., Johnson, R.G., Wright Jr., H.E., 1995. Glacial drainage towards the Mediterranean during the middle and late Pleistocene. *Boreas* 24, 196–206.
- Biedermann, A.R., Bender Koch, C., Lorenz, W.E.A., Hirt, A.M., 2014. Low-temperature magnetic anisotropy in micas and chlorite. *Tectonophysics* 629, 63–74. <https://doi.org/10.1016/j.tecto.2014.01.015>.
- Bradák, B., 2009. Application of anisotropy of magnetic susceptibility (AMS) for the determination of paleo-wind directions and paleo-environment during the accumulation period of Bag Tephra, Hungary. *Quat. Int.* 198, 77–84. <https://doi.org/10.1016/j.quaint.2007.11.005>.
- Bradák, B., Thamó-Bozsó, E., Kovács, J., Márton, E., Csillag, G., Horváth, E., 2011. Characteristics of Pleistocene climate cycles identified in Cérna Valley loess-paleosol section (Vértesacska, Hungary). *Quat. Int.* <https://doi.org/10.1016/j.quaint.2010.05.002>.
- Bradák, B., Újvári, G., Seto, Y., Hyodo, M., Végh, T., 2018a. A conceptual magnetic fabric development model for the Paks loess in Hungary. *Aeolian Res* 30, 20–31. <https://doi.org/10.1016/j.aeolia.2017.11.002>.
- Bradák, B., Seto, Y., Hyodo, M., Szeberényi, J., 2018b. Relevance of ultrafine grains in the magnetic fabric of paleosols. *Geoderma* 330, 125–135. <https://doi.org/10.1016/j.geoderma.2018.05.036>.
- Bradák, B., Kovács, J., Magyari, A., 2019. The origin and significance of some “irregular” loess magnetic fabric found in the Paks succession (Hungary). *Geophys. J. Int.* 217, 1742–1754. <https://doi.org/10.1093/gji/ggz117>.
- Branston, A.G., Livezey, R.E., 1987. Classification, seasonality, and persistence of low-frequency atmospheric circulation patterns. *Mon. Weather Rev.* 115, 1083–1126.
- Buggle, B., Glaser, B., Zöller, L., Hambach, U., Marković, S., Glaser, I., Gerasimenko, N., 2008. Geochemical characterization and origin of Southeastern and Eastern European loesses (Serbia, Romania, Ukraine). *Quat. Sci. Rev.* 27, 1058–1075. <https://doi.org/10.1016/j.quascirev.2008.01.018>.
- Buggle, B., Glaser, B., Hambach, U., Gerasimenko, N., Marković, S., 2011. An evaluation of geochemical weathering indices in loess-paleosol studies. *Quat. Int.* 240, 12–21. <https://doi.org/10.1016/j.quaint.2010.07.019>.
- Chadima, M., Jelínek, V., 2008. Anisoft 4.2 — anisotropy data browser. *Contrib. Geophys. Geodes.* 38 (special issue), 41.
- Chapman, M.R., Maslin, M.A., 1999. Low-latitude forcing of meridional temperature and salinity gradients in the subtropical North Atlantic and the growth of glacial ice sheets. *Geology* 27, 875–878.
- Dasog, G.S., Mermut, A.R., Acton, D.F., 1987. Micromorphology and submicroscopy of illuvial mineral particles in boreal clay soils of saskatchewan, Canada. *Geoderma* 40, 193–208.
- D'Arrigo, R., Jacoby, G., Wilson, R., Panagiotopoulos, F., 2005. A reconstructed Siberian High index since A.D. 1599 from Eurasian and North American tree rings. *Geophys. Res. Lett.* 32, 1–4. <https://doi.org/10.1029/2004GL022271>.
- Dubey, Ashok Kumar., 2014. Anisotropy of Magnetic Susceptibility. Springer Geology, pp. 17–34. https://doi.org/10.1007/978-3-319-05588-6_2.
- Goretskiy, G.I., 1958. About periglacial formation. *Bull. Quat. Commis.* 22, 3–23.
- Tarling, D.H., Hrouda, F., 1993. *The Magnetic Anisotropy of Rocks*. Chapman and Hall, London.
- Helland, P.E., Holmes, M.A., 1997. Surface textural analysis of quartz sand grains from ODP Site 918 off the southeast coast of Greenland suggests glaciation in southern Green-land at 11 Ma. *Palaeogeogr. Palaeoclimatol. Palaeoecol.* 135, 109–121.
- Hersbach, H., Bell, B., Berrisford, P., Hirahara, S., Horányi, A., Muñoz-Sabater, J., Nicolas, J., Peubey, C., Radu, R., Schepers, D., Simmons, A., Soci, C., Abdalla, S., Abellan, X., Balsamo, G., Bechtold, P., Biavati, G., Bidlot, J., Bonavita, M., De Chiara, G., Dahlgren, P., Dee, D., Diamantakis, M., Dragani, R., Flemming, J., Forbes, R., Fuentes, M., Geer, A., Haimberger, L., Healy, S., Hogan, R.J., Hólm, E., Janisková, M., Keeley, S., Laloyaux, P., Lopez, P., Lupu, C., Radnoti, G., de Rosnay, P., Rozum, I., Vamborg, F., Villaume, S., Thépaut, J.N., 2020. The ERA5 global reanalysis. *Q. J. R. Meteorol. Soc.* 146, 1999–2049. <https://doi.org/10.1002/qj.3803>.
- Hrouda, F., 1982. Magnetic anisotropy of rocks and its application in geology and geophysics. *Geophys. Surv.* 5, 37–82.
- Hunt, C.P., Banerjee, S.K., Solheid, P.A., Sun, W.-W., 1994. Rock-magnetic study of the climate proxy record at Xining in the Chinese loess plateau, north-central China (abstract). *Eos, Trans. AGU* 75 (44Suppl. 1), 187.
- Hus, J.J., 2003. The magnetic fabric of some loess/paleosol deposits. *Phys. Chem. Earth* 28, 689–699. [https://doi.org/10.1016/S1474-7065\(03\)00128-1](https://doi.org/10.1016/S1474-7065(03)00128-1).
- Ibrayev, R.A., Özsoy, E., Schrum, C., Sur, H.I., 2010. Seasonal variability of the Caspian

- Sea three-dimensional circulation, sea level and air-sea interaction. *Ocean Sci.* 6, 311–329. www.ocean-sci.net/6/311/2010/.
- Jelinek, V., 1977. The Statistical Theory of Measuring Anisotropy of Magnetic Susceptibility of Rocks and its Application.
- Jordanova, N., Jordanova, D., Karloukovski, V., 1996. Magnetic fabric of Bulgarian loess sediments derived by using various sampling techniques. *Studia Geophys. Geod.* 40, 36–49. <https://doi.org/10.1007/BF02295904>.
- Kislov, A.V., Panin, A., Toropov, P., Yank-Hombach, V., 2014. Current status and palaeostages of the Caspian Sea as a potential evaluation tool for climate model simulations. *Quat. Int.* 345, 48–55.
- Költringer, C., Stevens, T., Bradák, B., Almqvist, B., Kurbanov, R., Snowball, I., Yarovaya, S., 2020. Enviromagnetic study of Late Quaternary environmental evolution in Lower Volga loess sequences, Russia. *Quat. Res.* 1–25. <https://doi.org/10.1017/qua.2020.73>.
- Kurbanov, R.N., Murray, A.S., Yanina, T.A., Svistunov, M.I., Taratunina, N.A., Thompson, W.K., 2020. First optically stimulated luminescence ages of the early khvalynian Caspian sea transgression in the lower volga. *Boreas*.
- Kutiel, H., Benaroch, Y., 2002. North Sea-Caspian pattern (NCP) – an upper level atmospheric teleconnection affecting the Eastern Mediterranean: identification and definition. *Theor. Appl. Climatol.* 71, 17–28. <https://doi.org/10.1007/s704-002-8205-x>.
- Lagroix, F., Banerjee, S.K., 2002. Paleowind directions from the magnetic fabric of loess profiles in central Alaska. *Earth Planet Sci. Lett.* 195.
- Lagroix, F., Banerjee, S.K., 2004a. Cryptic post-depositional reworking in aeolian sediments revealed by the anisotropy of magnetic susceptibility. *Earth Planet Sci. Lett.* 224, 453–459. <https://doi.org/10.1016/j.epsl.2004.05.029>.
- Lagroix, F., Banerjee, S.K., 2004b. The regional and temporal significance of primary aeolian magnetic fabrics preserved in Alaskan loess. *Earth Planet Sci. Lett.* 225, 379–395. <https://doi.org/10.1016/j.epsl.2004.07.003>.
- Lagroix, F., Borradaile, G.J., 2000. Magnetic fabric interpretation complicated by inclusions in mafic silicates. *Tectonophysics* 325 (3), 207–225.
- Lavrushin, Y.A., Spiridonova, E.A., Tudryn, A., Chalie, F., Antipov, M.P., Kuralenko, N.P., Kurina, E.E., Tucholka, P., 2014. Kaspiy: gidrologicheskoye sobytiya pozdnego kvartera (The Caspian Sea: hydrological events of the late Quaternary). *Bull. Commiss. Study Quat.* 73, 19–51.
- Lebedeva, M., Makeev, A., Rusakov, A., Romanis, T., Yanina, T., Kurbanov, R., Kust, P., Varlamov, E., 2018. Landscape dynamics in the caspian lowlands since the last deglaciation reconstructed from the pedosedimentary sequence of srednaya akhtuba, southern Russia. *Geosciences* 8, 492. <https://doi.org/10.3390/geosciences8120492>.
- Liang, Y., Yang, T.B., Velichko, A.A., Zeng, B., Shi, P.H., Wang, L.D., He, Y., Chen, J., Chen, Y., 2016. Paleoclimatic record from Chumbur-Kosa section in Sea of Azov region since marine isotope stage 11. *J. Mt. Sci.* 13, 985–999.
- Lindner, M., Finger, F., 2018. Geochemical characteristics of the late proterozoic spitz granodiorite gneiss in the drosendorf unit (southern bohemian massif, Austria) and implications for regional tectonic interpretations. *J. Geosci.* 63, 345–362. <https://doi.org/10.3190/jgeosci.271>.
- Lisiecki, L.E., Raymo, M.E., 2005. A Pliocene-Pleistocene stack of 57 globally distributed benthic $\delta^{18}O$ records. *Paleoceanography* 20, PA1003.
- Liu, X.-M., Xu, T.-C., Liu, T.-S., 1988. The Chinese loess in Xifeng, II. A study of anisotropy of magnetic susceptibility of loess from Xifeng. *Geophys. J. Roy. Astron. Soc.* 92, 349–353.
- Mahaney, W.C., 1995. Glacial crushing, weathering and diagenetic histories of quartz grains inferred from scanning electron microscopy. In: Menzies, J. (Ed.), *Modern Glacial Environments - Processes, Dynamics and Sediments*. Butterworth-Heinemann Ltd, Oxford, pp. 487–506.
- Mahaney, W.C., 2002. *Atlas of Sand Grain Surface Textures and Applications*. Oxford University Press, p. 237.
- Matasova, G.G., Kazansky, A.Y., 2004. Magnetic properties and magnetic fabrics of Pleistocene loess/paleosol deposits along west-central Siberian transect and their palaeoclimatic implications. *Geol. Soc. Spec. Publ.* 238, 145–173. <https://doi.org/10.1144/GSL.SP.2004.238.01.11>.
- Matasova, G., Petrovský, E., Jordanova, N., Zykina, V., Kapička, A., 2001. Magnetic study of Late Pleistocene loess/paleosol sections from Siberia: palaeoenvironmental implications. *Geophys. J. Int.* 147, 367–380. <https://doi.org/10.1046/j.0956-540X.2001.01544.x>.
- McLennan, S.M., 1993. Weathering and global denudation. *J. Geol.* 101, 295–303.
- Mees, F., 2010. Authigenic silicate minerals – sepiolite-palygorskite, zeolites and sodium silicates. In: Stoops, G., Marcelino, V., Mees, F. (Eds.), *Interpretation of Micromorphological Features of Soils and Regoliths*. Elsevier, Amsterdam, pp. 497–520.
- Molavi-Arabshahi, M., Arpe, K., Leroy, S.A.G., 2016. Precipitation and temperature of the southwest Caspian Sea region during the last 55 years: their trends and teleconnections with large-scale atmospheric phenomena. *Int. J. Climatol.* 36, 2156–2172. <https://doi.org/10.1002/joc.4483>.
- Nawrocki, J., Polechońska, O., Boguckij, A., Łanczont, M., 2006. Palaeowind directions recorded in the youngest loess in Poland and western Ukraine as derived from anisotropy of magnetic susceptibility measurements. *Boreas* 35, 266–271. <https://doi.org/10.1080/03009480600584907>.
- Nawrocki, J., Gozhik, P., Łanczont, M., Pańczyk, M., Komar, M., Bogucki, A., Williams, I.S., Czupyt, Z., 2018. Palaeowind directions and sources of detrital material archived in the Roxolany loess section (southern Ukraine). *Palaeogeogr. Palaeoclimatol. Palaeoecol.* 496, 121–135. <https://doi.org/10.1016/j.palaeo.2018.01.028>.
- Nesbitt, H.W., Young, G.M., 1982. Early Proterozoic climates and plate motions inferred from major element chemistry of lites. *Nature* 299, 715–717.
- Nesbitt, H.W., Markovics, G., Price, R.C., 1980. Chemical processes affecting alkalis and alkaline earths during continental weathering. *Geochem. Cosmochim. Acta* 44, 1659–1666.
- Novothny, Á., Frechen, M., Horváth, E., Wacha, L., Rolf, C., 2011. Investigating the penultimate and last glacial cycles of the Sütto loess section (Hungary) using luminescence dating, high resolution grain size, and magnetic susceptibility data. *Quat. Int.* 234, 75–85.
- Panin, A., Matlakhova, E., 2015. Fluvial chronology in the East European Plain over the last 20 ka and its palaeohydrological implications. *Catena* 130, 46–61.
- Peng, S., Ge, J., Li, C., Liu, Z., Qi, L., Tan, Y., Cheng, Y., Deng, C., Qiao, Y., 2015. Pronounced changes in atmospheric circulation and dust source area during the mid-Pleistocene as indicated by the Caotan loess-soil sequence in North China. *Quat. Int.* 372, 97–107. <https://doi.org/10.1016/j.quaint.2014.09.075>.
- Pokorný, Jiří, Pokorný, Petr, Suza, Petr, Hrouda, F., 2011. A multi-function Kappa-bridge for high precision measurement of the AMS and the variations of magnetic susceptibility with field, temperature and frequency. *The Earth's Magnetic Interior*. <https://doi.org/10.1007/978-94-007-0323-0>.
- Pullen, A., Juan, R., Pecha, M., Gehrels, G., 2011. ROCK CRUSHING & WATER TABLE INSTRUCTION MANUAL. Arizona LaserChrom Center. <https://drive.google.com/file/d/0B9eZu34P5h8eYUW3MWMxOWMtMzgxNS00MDNjLTgzYjUtZDU0MmRkYTkxNGMw/view>.
- Reeder, S., Taylor, H., Shaw, R.A., Demetriades, A., 2006. Introduction to the chemistry and geochemistry of the elements. In: Tarvainen, T., de Vos, M. (Eds.), *Geochemical Atlas of Europe. Part 2. Interpretation of Geochemical Maps, Additional Tables, Figures, Maps, and Related Publications*. Geological Survey of Finland, Espoo, pp. 48–429.
- Rochette, P., 1987. Magnetic susceptibility of the rock matrix related to the magnetic fabric studies. *J. Struct. Geol.* 9, 1015–1020. [https://doi.org/10.1016/0191-8141\(87\)90009-5](https://doi.org/10.1016/0191-8141(87)90009-5).
- Rodionov, S.N., 2003. Water Science and Technology Library. <https://doi.org/10.1007/0-306-48065-4>.
- Schaffernicht, E.J., Ludwig, P., Shao, Y., 2019. Linkage between dust cycle and loess of the last glacial maximum in Europe. *Atmos. Chem. Phys. Discuss.* 1–27. <https://doi.org/10.5194/acp-2019-693>.
- Strand, K., Immonen, N., 2010. Dynamics of the Barents-Kara ice sheet as revealed by quartz sand grain microtextures of the Late Pleistocene Arctic Ocean sediments. *Quat. Sci. Rev.* 29, 3583–3589.
- Taratunina, N., Rogov, V., Streletskaya, I., Thomson, W., Kurchatova, A., Yanina, T., Kurbanov, R., 2020. Late Pleistocene cryogenesis features of a loess-paleosol sequence in the Srednyaya Akhtuba reference section, Lower Volga river valley, Russia. *Quat. Int.* <https://doi.org/10.1016/j.quaint.2020.12.015>.
- Taylor, S.N., Lagroix, F., 2015. Magnetic anisotropy reveals the depositional and post-depositional history of a loess-paleosol sequence at Nussloch (Germany): AMS of Nussloch loess-paleosol sequence. *J. Geophys. Res. Solid Earth* 120. <https://doi.org/10.1002/2014JB011803>.
- Tudryn, A., Chalié, F., Lavrushin, Y.A., Antipov, M.P., Spiridonova, E.A., Lavrushin, V., Tucholka, P., Leroy, S.A.G., 2013. Late quaternary Caspian sea environment: late khazarian and early khvalynian transgressions from the lower reaches of the Volga River. *Quat. Int.* 292, 193–204. <https://doi.org/10.1016/j.quaint.2012.10.032>.
- Van Vliet-Lanoë, B., 2010. Frost action. In: Stoops, G., Marcelino, V., Mees, F. (Eds.), *Interpretation of Micromorphological Features of Soils and Regoliths*. Elsevier, Amsterdam, pp. 81–108.
- Vos, K., Vandenbergh, N., Elsen, J., 2014. Surface textural analysis of quartz grains by scanning electron microscopy (SEM): from sample preparation to environmental interpretation. *Earth Sci. Rev.* 128, 93–104. <https://doi.org/10.1016/j.earscirev.2013.10.013>.
- Williams, P.J., Smith, M.W., 1989. *The Frozen Earth: Fundamentals of Geocryology*. Cambridge Univ. Press, New York, p. 306.
- Yanina, T.A., 2014. The Ponto-Caspian region: environmental consequences of climate change during the Late Pleistocene. *Quat. Int.* 345, 88–99. <https://doi.org/10.1016/j.quaint.2014.01.045>.
- Yanina, T.A., Svistunov, M.I., Kurbanov, R., Murray, A.S., Tkach, N.T., Sychev, N.Y., 2017. Paleogeographic analysis of the results of optically stimulated luminescence dating of pleistocene deposits of the lower volga area. *Vestn. Mosk. Univ. Seriya 5 Geogr.* 2017-Janua 20–28.
- Zhang, R., Kravchinsky, V.A., Zhu, R., Yue, L., 2010. Paleomonsoon route reconstruction along a W-E transect in the Chinese Loess Plateau using the anisotropy of magnetic susceptibility: summer monsoon model. *Earth Planet Sci. Lett.* 299, 436–446. <https://doi.org/10.1016/j.epsl.2010.09.026>.
- Zhu, R., Liu, Q., Jackson, M.J., 2004. Palaeoenvironmental significance of the magnetic fabrics in Chinese loess-paleosols since the last interglacial (< 130 ka). *Earth Planet Sci. Lett.* 221, 55–69. [https://doi.org/10.1016/S0012-821X\(04\)00103-7](https://doi.org/10.1016/S0012-821X(04)00103-7).